DELFT UNIVERSITY OF TECHNOLOGY

MASTER THESIS

The Measurement of the X(3872) production cross section via decays to $J/\psi\pi^+\pi^-$ in pp collisions at $\sqrt{s} = 13$ TeV

Author:
Bo HEIJN

Supervisor:
Dr. Patrick KOPPENBURG

A thesis submitted in fulfillment of the requirements for the degree of MSc Applied Physics

in the

LHCb experiment
Nikhef

May 14, 2018

DELFT UNIVERSITY OF TECHNOLOGY

Abstract

Nikhef

MSc Applied Physics

The Measurement of the X(3872) production cross section via decays to $J/\psi\pi^+\pi^-$ in pp collisions at $\sqrt{s} = 13$ TeV

by Bo HEIJN

Production of the $X(3872)$ is studied in pp collisions at $\sqrt{s} = 13$ TeV using decays to $J/\psi\ \pi^+\pi^-$. A double-differential production cross section for the total, prompt and non prompt component is presented. The cross section is normalised to that of $\psi(2S)$ and done in 10 bins of transverse momentum ($5 < p_{\mathrm{T}} < 15$ GeV/c) and 5 bins of rapidity ($2.5 < y < 4$). In addition an unbinned production cross section on the non prompt component is presented in order to investigate the fraction of $X(3872)$ produced from B_c^+.

Abstract **i**

1 Introduction **1**
1.1 Previous measurements 3
1.2 Method 5

2 Data **7**
2.1 LHCb 7
2.2 Selection process 8
Stripping lines and reconstruction 9
Further offline candidate Selection 12

3 The model **17**
3.1 Mass 17
3.2 Pseudo proper time 18
3.3 2D model 21

4 Results **22**
4.1 Binned 2D fit 22
4.2 Non prompt $X(3872)$ 27

5 Conclusion and Discussion **32**

A Parameters 2D fit **33**

B References **38**
References 38

1 Introduction

Among the particles discovered during the last two decades, the famous Higgs boson has a special role as the last discovered building block of the standard model of particle physics. It was long anticipated as it was predicted by François Englert, Robert Brout [1] and Peter Higgs [2], in 1964.

However, most of the particles discovered in the last two decades were very unexpected and seem to be connected. They are called *exotic hadrons*. Hadrons are particles made up of quarks. They are called exotic because they were unexpected and did not fit in the picture of the particles discovered until then.

Hundreds of composite particles are known. Until 2003 all of these were either mesons, pairs of a quark and anti-quark, or baryons, triplets of quarks. The states we're interested in are states composed of (at least) one charm quark and a charm anti-quark. Such systems are called charmonium and are known and studied since the November revolution in 1974, which was ignited by the discovery of the J/ψ meson. The J/ψ is the most common form of charmonium due to its low rest mass and narrow width. After the discovery of this J/ψ, more (excited) states of charmonium have been found, with the assumption that all charmonium states are $c\bar{c}$ states. These states were anticipated and expected to have a close analogy with positronium or the hydrogen atom. This analogy is the one-to-one correspondence between the allowed states. The predicted states differ by their mass, and are characterised by their spin (S) and angular momentum (L). Like the hydrogen atom you can then organise them by their quantum numbers J^{PC} with $J = L + S$, the parity $P = (-1)^{L+1}$ and charge-conjugation $C = (-1)^{L+S}$ eigenvalues (see Fig. **??**).

This simple picture, however, was upset by the observation of the so-called $X(3872)$ meson at the Belle experiment [3]. It does not fit the picture outlined above and thus could be a four-quark state. Since then several other potential four-quark states have been observed, both neutral and charged. A good chronology can be found in Ref. [4]. All allowed states are shown in Fig. 1.2 and 1.3 in black (if found) and blue (if not yet). Any observed state that does not fit this picture is "exotic", and marked in red. The neutral $X(3872)$ meson appears at $J^{PC} = 1^{++}$ and the pentaquarks observed by LHCb [5] at the right of the charged section.

How can such exotic states occur? By putting quarks and gluons together; any multiple of three quarks (number of quarks minus anti-quarks), plus any number of gluons can be put together to get a valid colourless hadron. They can also be organised as a molecular system of mesons or as compact objects (see Fig. 1.1).

Which of these quark configurations are realised in Nature is unknown. It is also not yet possible to unambiguously assign any of these exotic states to a given quark configuration. More measurements of the properties of exotic hadrons are required. There may even be several configurations at play simultaneously: the $X(3872)$ meson behaves like a $\bar{D}D^{*0}$ molecule, but also like regular $c\bar{c}$ charmonium. So it may even be a quantum superposition of a molecule and the yet undiscovered $\chi_{c_1}(2P)$ charmonium state.

While $X(3872)$ meson was observed in b-hadron (hadrons containing a b quark) decays, its observation at the LHC [6–8] has shown that it is possible to promptly

- Hadron
  - Conventional states
    - Meson : $q\bar{q},\ Q\bar{q},\ Q\overline{Q}$
    - Baryon : $qqq,\ Qqq,\ QQq,\ QQQ$
  - Exotic states
    - Molecular state: $(Q\overline{q})(\overline{Q}q), (q\overline{q})(\overline{q}q)\ldots$
    - Hybrid meson: $Q\overline{Q}g, q\overline{q}g\ldots$
    - Glueball: gg
    - Tetra-pentaquark
      - Compact: $Q\overline{q}\overline{Q}q, Q\overline{Q}\overline{q}qq\ldots$
      - Diquark-antidiquark: $(Qq)(\overline{Q}\overline{q})\ldots$
      - Triquark-antidiquark: $(Qqq)(\overline{Q}\overline{q})\ldots$
      - ...

FIGURE 1.1: Possible configurations of quarks. Here q is used for the lighter quarks while Q is used for the heavier b or c quarks. The g is a gluon.

produce and reconstruct exotic hadrons at the LHC. Meaning they are directly produced upon collision of the protons and are not a product of other decaying particles which áre promptly produced. This simple fact has implications on its nature. Diquark and hadro-quarkonium models (non molecular systems) predict a larger production cross-section. They also predict harder p_{T} spectra than molecular model [9]. Therefore a study of the transverse momentum (p_{T}) distribution of $X(3872)$ meson is a strong test of models. This topic is hotly debated on `arXiv`, as can be seen from a recent thread of preprints [10].

It is however not surprising that the observation that $X(3872)$ is promptly produced was performed with the $X(3872)$ state only and so far with none of the many other exotic hadrons, as it was found in six decay modes and both in b-hadron decays and hadron collisions. This makes the $X(3872)$ meson special among exotic hadrons and is the reason that it is well studied. Because $X(3872)$ allows for many studies to be performed it plays a central role in exotic spectroscopy and even though its nature is still disputed, a lot is known about its mass, which is exactly that of a $\bar{D}^0 D^{*0}$ system $m_{X(3872)} - m_{\bar{D}^0} - m_{D^{*0}} = 0.01 \pm 0.19\,\mathrm{MeV}/c^2$ [11], its decay width, which is unexpectedly narrow, its quantum numbers, $J^{PC} = 1^{++}$ [12], and its allowed decays, which indicate that it cannot be a classical charmonium nor a $c\bar{c}g$ hybrid.

There is also a weak indication to be cross-checked, that the $X(3872)$ meson is produced in B_c^+ meson decays at a rate higher than expected [8]. The idea is not outrageous: we do not know what the $X(3872)$ is and how it is produced. It may be enhanced when both charm quarks are on the same side of the W with respect to the usual $b \to cW(\to \bar{c}s)$ decays. The former is the preferred production mechanism in B_c^+ decays as it is neither CKM nor colour suppressed (Fig. 1.4).

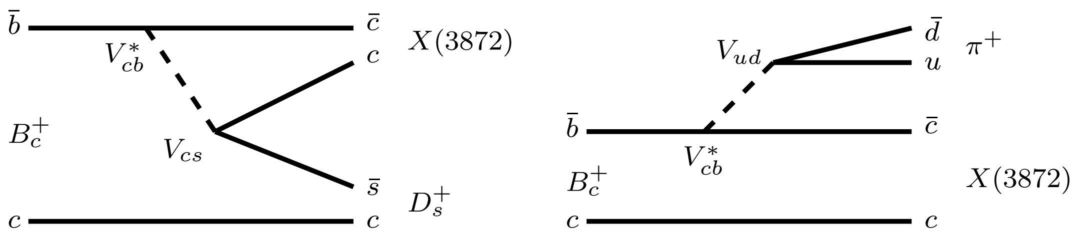

FIGURE 1.4: Example Feynman diagrams for $B_c^+ \to X(3872)$... decays. (left) The colour-suppressed diagram is the only topology accessible in B^+ and B_s^0 decays, while (right) the spectator-side production is only available in B_c^+ decays as it already contains a c. These diagrams assume that the $X(3872)$ meson is formed from a $c\bar{c}$ pair.

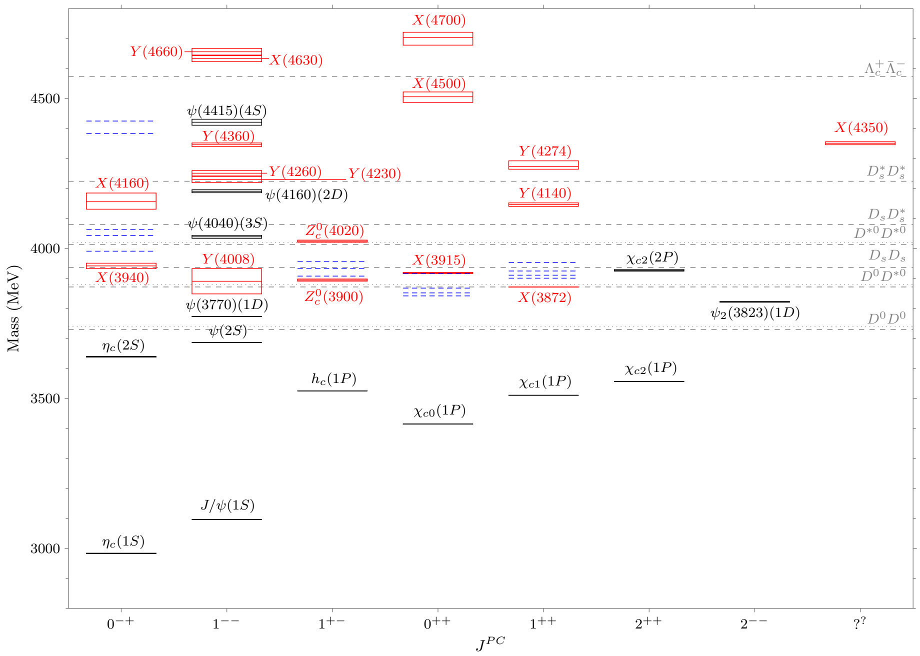

FIGURE 1.2: Mass spectrum of charmonium states versus quantum numbers J^{PC} for neutral charged states. Observed conventional states are indicated in black, yet unobserved conventional states in blue and observed exotic states in red. Boxes indicate wide states. The dashed lines indicate two-meson thresholds.

1.1 Previous measurements

Three measurements have been performed at the LHC, summarised in Table 1.1

LHCb was first to observe $X(3872)$ production at the LHC [6], using 2010 data. The paper reports a total cross-section times branching fractions in the fiducial volume of $5.4 \pm 1.3 \pm 0.8$ nb and a mass measurement. The mass plot is shown in Fig. 1.5.

CMS used the 2011 data to perform a measurement of the ratio of $X(3872)$ to $\psi(2S)$ production and used the flight distance to determine the non-prompt fraction (around 30%) [7].

ATLAS performed a similar measurement with 8TeV 2012 data [8] and confirmed the non-prompt fraction, which is largely independent of p_{T}.

TABLE 1.1: Available $X(3872)$ production measurements at the LHC.

Experiment	$\sqrt{s}$	Fiducial region	Data size	Yield
LHCb [6]	7 TeV	$2.5 < y < 4.5, 5 < p_{\mathrm{T}} < 20\,\mathrm{GeV}/c$	$35\,\mathrm{pb}^{-1}$	565 ± 62
CMS [7]	7 TeV	$\lvert y \rvert < 1.2, 10 < p_{\mathrm{T}} < 50\,\mathrm{GeV}/c$	$4.8\,\mathrm{fb}^{-1}$	$11\,910 \pm 490$
ATLAS [8]	8 TeV	$\lvert y \rvert < 0.75, 10 < p_{\mathrm{T}} < 70\,\mathrm{GeV}/c$	$11.4\,\mathrm{fb}^{-1}$	$\sim 60\,000$

Performing a three-component fit to the lifetime distribution, ATLAS found a surprisingly large fraction of non prompt $X(3872)$ from B_c^+ decays: $25 \pm 12 \pm 2 \pm 5$ (spin)% [8] (Fig. 1.5).

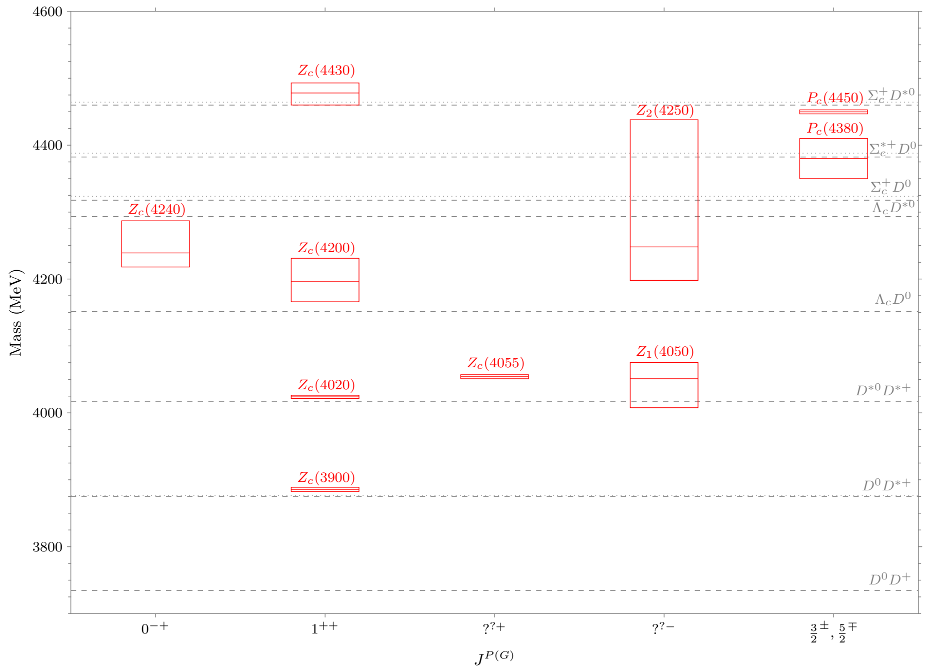

FIGURE 1.3: Mass spectrum of charmonium states versus quantum numbers J^{PC} for charged states. Observed conventional states are indicated in black, yet unobserved conventional states in blue and observed exotic states in red. Boxes indicate wide states. The dashed lines indicate two-meson thresholds.

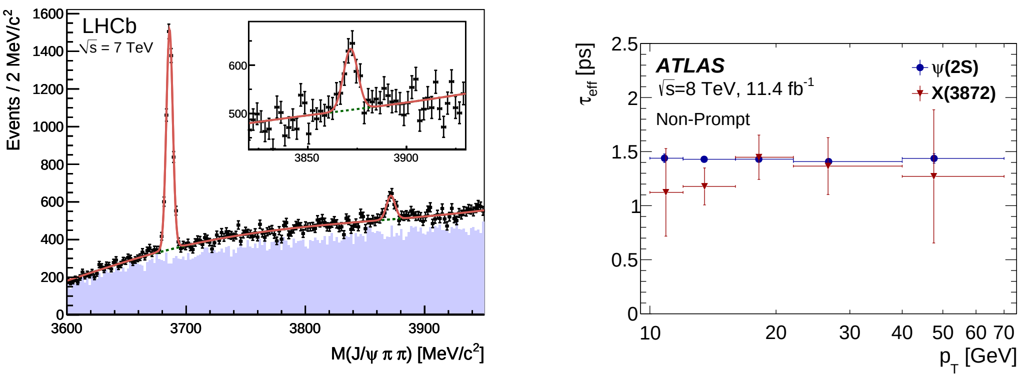

FIGURE 1.5: (left) Mass distribution of $J/\psi\pi^+\pi^-$ candidates in Ref. [6]. (right) Average lifetime on non-prompt $X3872$) and $\psi(2S)$ versus p_{T} [8].

LHCb has measured the B_c^+-to-B^+ production cross-section at 8 TeV as [13]

$$\frac{\sigma(B_c^+)\mathcal{B}(B_c^+ \to J/\psi\,\pi^+)}{\sigma(B^+)\mathcal{B}(B^+ \to J/\psi\,K^+)} = 0.683 \pm 0.018 \pm 0.009\% \tag{1.1}$$

Assuming that $\mathcal{B}(B_c^+ \to J/\psi\,\pi^+) \simeq 3\times10^{-3}$ [14] and $\mathcal{B}(B^+ \to J/\psi\,K^+) \simeq 1\times10^{-3}$ [11] one gets

$$\begin{aligned}\frac{\sigma(B_c^+)\times 3\times10^{-3}}{\sigma(B^+)\times10^{-3}} &= 0.683\pm0.018\pm0.009\% \\ \frac{\sigma(B_c^+)}{\sigma(B^+)} &\simeq 0.23\ \%.\end{aligned} \tag{1.2}$$

Furthermore, the relative production rate of b-hadrons are described by the fragmentation fraction $f(B_0)$, $f(B^+)$, $f(B_s^0)$ and $f(\Lambda_b^0)$, which describe the probability that a b quark fragments into that specific particle. There are of course more b hadrons known, however these are much less abundantly produced and therefore we assume $f(B_0)+f(B^+)+f(B_s^0)+f(\Lambda_b^0) \simeq 1$. Under the assumption of isospin symmetry we can assume $f(B_0) = f(B^+)$. From Ref. [15–17] we know $f(\Lambda_b^0)/f(B_0) \simeq 0.808$ and $f(B_s^0)/f(B_0) \simeq 0.26$. This gives $f(B_0) \simeq 1/2.66 = 0.38$. And so, when we put this in (1.2), we get $f(B_c^+) = 0.075\%$ or less than one in thousand b-hadrons is a B_c^+ meson. This makes the central value obtained by ATLAS very unlikely as it would mean there is an enhancement by two orders of magnitude of the $X(3872)$ production in B_c^+ mesons.

In this thesis this claim has been checked with LHCb data.

1.2 Method

We performed a differential cross-section measurement of X(3872) $\to J/\psi\,\pi^+\pi^-$, where $J/\psi \to \mu^+\mu^-$. This measurement was done in pp collisions at $\sqrt{s} = 13\,\text{TeV}$. This is the first time a $X(3872)$ cross-section measurement at 13 TeV has been done.

Alike that of the J/ψ measurement in Ref. [18], this measurement was done in bins of rapidity y and transverse momentum (p_{T}). The cross-sections were normalised to that of the $\psi(2S)$ meson, which decays to the same final state, so practically measuring

$$\frac{\frac{\mathrm{d}\sigma}{\mathrm{d}\eta\mathrm{d}p_{\mathrm{T}}}(pp\to X(3872))\times\mathcal{B}(X(3872)\to J/\psi\,\pi^+\pi^-)}{\frac{\mathrm{d}\sigma}{\mathrm{d}\eta\mathrm{d}p_{\mathrm{T}}}(pp\to \psi(2S))\times\mathcal{B}(\psi(2S)\to J/\psi\,\pi^+\pi^-)}, \tag{1.3}$$

where $\mathcal{B}$ stands for the branching fraction. This measurement was done by performing a two-dimensional fit in the pseudo-proper time and the corrected mass, $m_{J/\psi\,\pi^+\pi^-}$.

The pseudo-proper time is defined as

$$t_z = A_{\mathrm{ps}}\frac{m_{J/\psi\,\pi^+\pi^-}}{p_z}(z_{J/\psi\,\pi^+\pi^-} - z_{\mathrm{PV}}), \tag{1.4}$$

where $z_{J/\psi\,\pi^+\pi^-}$ and z_{PV} are the positions of the decay and primary pp vertices measured in mm, and $m(\mathrm{MeV/c^2})$ and $p_z(\mathrm{MeV/c})$ are the rest mass and third component of the $J/\psi\,\pi^+\pi^-$ candidate's four-momentum respectively. The factor $A_{\mathrm{ps}} = \frac{2.998}{10}$ is added to set the units of t_z to ps:

$$\begin{aligned} t_z &= A_{\text{ps}} \frac{m_{J/\psi\,\pi^+\pi^-}}{p_z} (z_{J/\psi\,\pi^+\pi^-} - z_{\text{PV}}) \\ &\equiv A_{\text{ps}} \frac{\text{MeV}/c^2\,\text{mm}}{\text{MeV}/c} \\ &\equiv A_{\text{ps}} \frac{10^{-3}\,\text{m}}{c} \\ &\equiv \frac{2.998 * 10^{-3}}{2.998 * 10^{9}}\,\text{s} \\ &= 10^{-12}\,\text{s} \end{aligned} \tag{1.5}$$

This pseudo-proper time basically gives the lifetime of its “mother" particle. For $t_z \simeq 0$ it is produced promptly at the primary pp vertices and for $t_z > 0$ it is the product of a decaying particle (non prompt). Thus it is used to disentangle the data between mesons produced in the pp collision and those coming from decays of b hadrons, yielding

$$\frac{\frac{\mathrm{d}\sigma}{\mathrm{d}\eta \mathrm{d}p_{\mathrm{T}}}(pp \to b \to X(3872)\ldots) \times \mathcal{B}(X(3872) \to J/\psi\,\pi^+\pi^-)}{\frac{\mathrm{d}\sigma}{\mathrm{d}\eta \mathrm{d}p_{\mathrm{T}}}(pp \to b \to \psi(2S)\ldots) \times \mathcal{B}(\psi(2S) \to J/\psi\,\pi^+\pi^-)}. \tag{1.6}$$

The corrected mass is defined by

$$m_{J/\psi\,\pi^+\pi^-} = m(\pi^+\pi^-\mu^+\mu^-) - m(\mu^+\mu^-) + m(J/\psi) \tag{1.7}$$

where the reconstructed mass for $\mu^+\mu^-$ is corrected for the known mass of the J/ψ. In Fig. 2.5a the distribution for the reconstructed mass of J/ψ can be seen. It has a resolution and also some background. Replacing this by the known value thus reduces the uncertainty in the data approximately by a factor 2 (assuming $\pi^+\pi^-$ has a similar resolution).

In addition, we performed an unbinned two-dimensional fit focussed on the area around $X(3872)$ to measure the non prompt production of $X(3872)$ more accurately. This will permit testing the ATLAS claim of enhanced B_c^+ production. ATLAS did not fit the lifetime distribution, but rather applied a cut on the flight distance. The method proposed here is more precise and will permit a better separation of the B_c^+ and of the b-hadron components.

In the proceeding sections we shall describe how the data is acquired and determine the optimal candidate selection of our data. We shall apply certain cuts and show why these cuts are justified based on simple models fitted on the corrected mass spectrum. We shall then proceed to build our full two-dimensional model, stating all components, their parameters and physical interpretation modeling the data. Finally we shall present our results and conclusions found during this research.

2 Data

To make a useful analysis we need many statistics. But where does all this data come from? The Large Hadron Collider (LHC) is the world's largest and most powerful particle accelerator. It is located at CERN (Conseil Européen pour la Recherche Nucléaire), Geneva. It first started up on 10 September 2008, and remains the latest addition to CERN's accelerator complex. The LHC consists of a 27-kilometre ring of superconducting magnets with a number of accelerating structures to boost the energy of the particles along the way. Inside the accelerator, two high-energy beams of (in our case) protons travel with a velocity nearing that of the speed of light before they collide. The beams travel in opposite directions in separate beam pipes both kept at ultrahigh vacuum.

2.1 LHCb

The Large Hadron Collider beauty (LHCb) experiment is one of the four main experiments collecting data from the LHC and is located at point 8 (see Fig. 2.1). LHCb involves around 700 scientist from 52 institutions around the globe. LHCb has recorded the particles produced by the first circulating proton beams at the LHC on October 10th, 2008.

The primary aim is to record the decay of particles containing b and $\bar{b}$ (anti-b) quarks or 'beauty quarks', hence the name Large Hadron Collider *beauty*. Particles containing a beauty quark are collectively known as b-hadrons. They are very unstable and short-lived, decaying into a range of other particles. But why are we interested in these b- hadrons?

The Big Bang should have created an equal amount of matter and anti-matter in the very early universe. But when we look around us we can only conclude that everything we see is built up almost entirely from matter. In fact, there is hardly any anti-matter to be found. So what happened to all the anti-matter? Why is there this so-called asymmetry? This is one of the greatest questions that physicists have yet to answer. And although beauty quarks are absent from the Universe in present times, they were abundant in the aftermath of the Big Bang. At the LHC they are also produced in vast quantities along with their anti-matter counterparts. And so it is believed that by analysing the decays of these beauty-quarks scientist of LHCb may be able to gain useful insights in where this asymmetry originates.

At the location of LHCb the proton beams pass through the experiment's 4,500 tonne detector (Fig. 2.1) located 100 metres under the ground. This detector is specifically designed to filter out these b-hadrons and the products of their decay. The detector consists of several subdetectors, each specialised in measuring different characteristics of the particles produced by colliding protons.

VELO The Vertex Locator. This is the part of the detector in which the proton beams collide. It consist of 42 silicon detector elements positioned extremely close to the primary vertex, the point where the protons collide. It's job is to select the b-hadrons from all the other particles and determine the distance between the point where the b-hadrons are created and where they decay. They are never measured directly. The VELO measures products of the *b*-hadrons' decay. From this it can locate the position of the *b*-hadron to within 10 μm.

RICH Ring Imaging Cherenkov detectors. These detectors are also designed to identify particles. They are located on either side of LHCb's magnet. This position is chosen in such a way that it is able to intercept particles flying at different speeds and angles. Their measurement is based on the detection of Cherenkov radiation. The amount of radiation depends on a particles speed. Thus RICH detectors determine the speed of particles.

Magnet The LHCb magnet consists of two coils, both weighing 27 tonnes, mounted inside a 1450 tonne steel frame. Each coil is constructed from 10 layers, wound from approximately 3 kilometres of aluminium cable. The magnet is there to help identify all the particles produced upon collision of the protons.

Tracking system The tracking system consists of four rectangular stations. Each station covers an area of approximately $40\,\mathrm{m}^2$. There are two different types of trackers used at LHCb. A *silicon tracker* which uses silicon microstrip detectors to detect passing particles. Charged particles collide with silicon atoms, kicking out electrons. These electrons create an electric current, which are measured. This tracker is placed close to the pipeline. The *outer tracker* is situated further from the pipeline. It is made up of thousands of gas-filled tubes. The gas inside these tubes becomes ionised when charged particles pass through it. The freed electrons are then again measured. Through these tracking systems the trajectory of the particles can be determined.

Calorimeters The calorimeters are designed to measure the amount of energy a particle loses when stopping them. There are two types of calorimeters at LHCb. The *electromagnetic calorimeter* ECAL and the *hadron calorimeter* HCAL. ECAL is responsible for measuring the energy of mainly electrons and photons, hence electromagnetic. HCAL is designed to determine the energy of hadrons passing through, hence hadronic.

Muon system The muon system is similar to the tracking system but then specifically for identifying muons. It consists of five rectangular stations with a combined area of $435\,\mathrm{m}^2$. The stations contain a combination of gassed which react with passing muons. Electrodes can then detect the results.

Together all these systems can determine the trajectory, velocity, charge, energy, mass and thus identity of the particles passing through. Inside the VELO the proton beams currently collide with such a velocity that upon collision they have a center of mass energy ($\sqrt{s}$) of 13 TeV. These collisions produce a vast amount of particles, "spraying" through the detector. Obviously we (i.e. for this research) are not interested in most of these. Both $\psi(2S)$ and $X(3872)$ decay into $J/\psi\,\pi^+\pi^-$ and J/ψ decays into $\mu^+\mu^-$. So the first step in the data processing must be only selecting all the particles μ^+, μ^-, π^+ and π^-. There are several steps in this selection process.

2.2 Selection process

The beams of protons travel in packets. Each beam (clockwise and counterclockwise) consist of approximately 2000 packets and these packets in turn hold up to approximately 10^{11} protons. During the run time of the LHC, the detectors of the

VELO produce data at a frequency of 15 MHz. However, there are only enough resources to store 10 kHz. So the first aim is to select the most relevant data to reduce it to 10 kHz. This first selection is done by the so called *trigger system*. The first level of the trigger system, *level zero trigger* reduces the frequency of data to about 1 MHz through a field programmable gate array (FPGA). This consist of preprogrammed chips designed to select the candidates above a certain p_{T} and pass this selection on to the next level. An important aspect is that it makes it's decision within 4 ms in order to be in time for the next event. This process uses the fact that particles from a B decay have a higher p_{T} with respect to the particle beam axis than particles coming directly from the primary proton-proton interaction. The second level of the trigger system, *high level trigger* (HLT) is divided into two sublevels. The first of these sublevels (Hlt1) then confirms these high p_{T} candidates of the level zero trigger and together with additional information reduces the amount of data to the order of 100 kHz. The second sublevel (Hlt2) of the HLT then has enough processing time to further decrease the amount of data to 10 kHz and run a reconstruction of the events. Their paths can be reconstructed because of the multiple layers of detectors. Through these reconstructed paths of each of these decays, a great amount of observables can be deduced like mass, momentum, direction and location. All these reconstructed paths are then organised in to groups belonging to certain decays. These groups are called *trigger lines*.

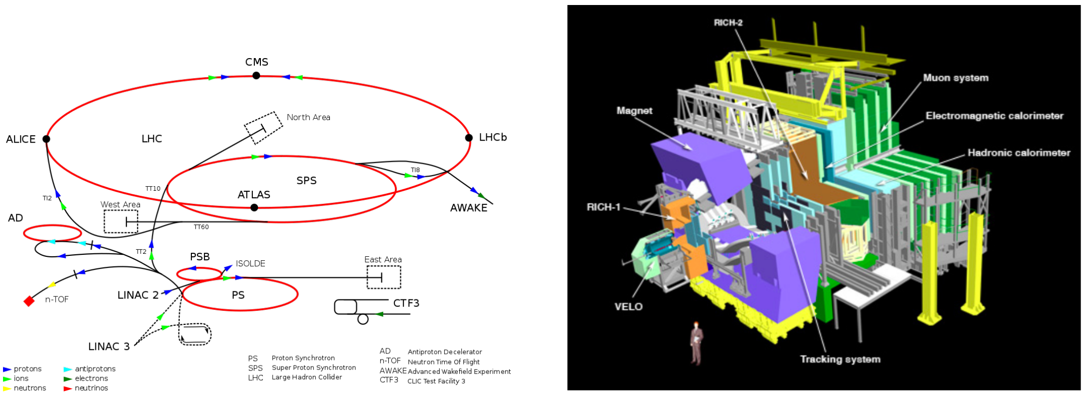

FIGURE 2.1: (left) Map of CERN accelerator complex showing the LHC and location of among others LHCb. (right) The detector with it's subdetectors.

Stripping lines and reconstruction

The data-taking strategy has considerably varied through the Run 2 period. Six independent samples from 2016 and 2017 are being used for the cross-section measurement with a combined integrated luminosity of 2435.59 pb^{-1}:

- X3872-2016-S28-Down-1580-1585-Small.root (837.72 pb^{-1})
- X3872-2016-S28-Up-1579-1586-1587-Small.root (790.47 pb^{-1})
- X3872-2017-S29-Down-1591-1598-Small.root (179.33 pb^{-1})
- X3872-2017-S29-Up-1590-1597-Small.root (220.55 pb^{-1})
- X3872-2017-S29r1-Down-1589-1596-Small.root (306.25 pb^{-1})
- X3872-2017-S29r1-Up-1588-1595-Small.root (101.25 pb^{-1}).

The following selection procedures were performed.

2016 & 2017: For 2016 data stripping 28 was used. The line used in 2016 was then heavily prescaled in 2017. Instead, Stripping 29 and 29r1 is used, thanks to the `FullDSTDiMuonJpsi2MuMuTOSLine`

```
"Prescale"      : 1.0,
"InputDiMuon"   : "StdLooseJpsi2MuMu",
"Cuts"          : {
  "MuonP"         : "MINTREE('mu+'==ABSID,P) > 10 *GeV",
  "JpsiPt"        : "PT > 3 *GeV",
  "Mass"          : "(MM > 3010) & (MM < 3170)",
  "MuonPIDmu"     : "MINTREE('mu+'==ABSID,PIDmu) > 0.0",
  "TOSL0"         : "TOS('L0.*Mu.*Decision', 'L0TriggerTisTos')",
  "TOSHlt1"       : "TOS('Hlt1DiMuonHighMassDecision',
                         'Hlt1TriggerTisTos')",
  "TOSHlt2"       : "TOS('Hlt2DiMuonJPsiHighPTDecision',
                         'Hlt2TriggerTisTos')",
  }
},
```

This line applies a cut on the transverse momentum of the J/ψ at $p_T > 3\,\mathrm{GeV}/c$. It also applies a cut on the p_T of the potential muons throwing away al candidates with $p < 10\,\mathrm{GeV}$. This is done because for low p_T the particles may get stopped earlier due to the material properties of the detector, which gives rise to higher probability of misidentification of the muon by for example pions. Furthermore it discards all potential muons for which the likelihood is larger of it being a pion. When the likelihood of being a muon is larger than the likelihood for being a pion the likelihood is also larger than the likelihood of being a proton or a kaon. Electrons are not considered because most of electrons produced get stopped by ECAL thus do not get mis-identified. Finally it checks three times that the J/ψ detected is triggered in the level zero trigger by two muons instead of a different particle. It does this at the zero lever trigger, Hlt1 and Hlt2. Each succesive level being more precise than the other due to longer processing times.

The data is then used to build $X(3872)$ candidates in a user job. This is done by looking for a pion pair which possibly originated from the same points as the muons.

```
_Jpsi = DataOnDemand( Location =
      'Dimuon/Phys/FullDSTDiMuonJpsi2MuMuTOSLine/Particles' )
JpsiCut = "(PT>3500*MeV)"
_pions = DataOnDemand( Location = 'Phys/StdAllLoosePions/Particles' )
piCut = "(PT>0.5*GeV)"
Psi2S = CombineParticles("Psi2S",
                         DecayDescriptor = 'psi(2S) -> J/psi(1S) pi+ pi-',
                         DaughtersCuts = { "pi+" :  piCut,
                                           "J/psi(1S)" : JpsiCut },
                         CombinationCut = "(AM>3450*MeV) &
                                           (AM<4150*MeV) &
                                           (ADOCACHI2CUT(25, ''))",
```

```
                                MotherCut = "(VFASPF(VCHI2)<45) &
                                            (M>3500*MeV) &
                                            (M<4100*MeV)")  # 45=9*5
SelPsi2S = Selection("SelPsi2S", Algorithm = Psi2S,
                          RequiredSelections = [ _Jpsi, _pions  ])
SeqPsi2S = SelectionSequence("SeqPsi2S", TopSelection = SelPsi2S)
```

In this user job first we look for all particles which could be a pion. We keep only the pions that have PID of $P[\pi] > 0.3$. That is, the chance that the particle identified as a pion is in fact a pion must be larger than 30%. Then we apply a cut keeping only the possible pions for which $p_T > 0.5\,\text{GeV}/c$. Afterwards we delete all candidates which overlap with the muons saved in the stripping (they can't be both) and combine them with the muons to reconstruct the $X(3873)$. Then after the reconstruction of all these events we keep only those that have a $\chi^2 < 45$ for the vertex of the $J/\psi\,\mu^+\mu^-$. As χ^2 is an indicator for the quality of the reconstructed event, this cut throws away pairs of $\mu^+\mu^-$ and $\pi^+\pi^-$ that most likely did not originate from the same vertex. Although $\chi^2 < 45$ is a pretty loose cut, tightening would not increase the precision as prompt $\mu^+\mu^-$ and $\pi^+\pi^-$ all come from the same vertex and thus would have a χ^2 close to 1 per degree of freedom even though they did not come from either J/ψ, $\psi(2S)$ or $X(3872)$.
We then apply a cut on the mass of this reconstructed $X(3872)$ to lie between 3500 and 4100 MeV/c^2. Once this is done we can plot the mass for all reconstructed candidates for $X(3872)$(Fig. 2.2a). In Fig. 2.2b we plotted the corrected mass and immediately the benefits can be seen in comparison to the reconstructed mass. We see the peak for the $\psi(2S)$ at $m_{J/\psi\,\mu^+\mu^-} = 3686\,\text{MeV}/c^2$ and the smaller but still clearly visible $X(3872)$ at approximately $m_{J/\psi\,\mu^+\mu^-} = 3872\,\text{MeV}/c^2$. For this thesis we consider the rest as background.

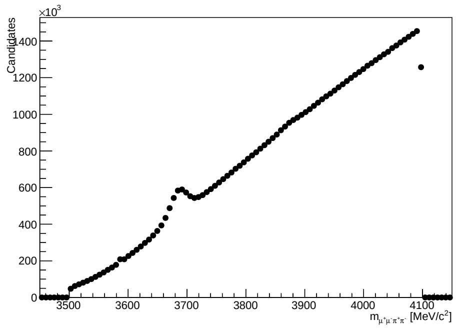

(A) Plot of the mass of all the reconstructed candidates possibly decaying into $\mu^+\mu^-\pi^+\pi^-$ that satisfy the conditions of the stripping/reconstruction procedure.

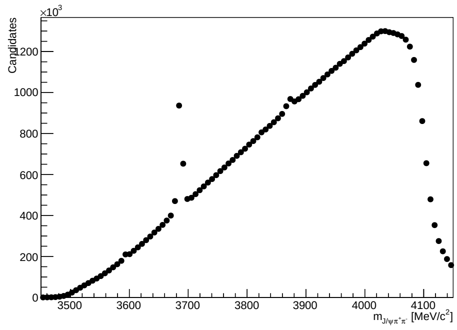

(B) Plot of the corrected mass of all the reconstructed candidates possibly decaying into $\mu^+\mu^-\pi^+\pi^-$ that satisfy the conditions of the stripping/reconstruction procedure.

FIGURE 2.2

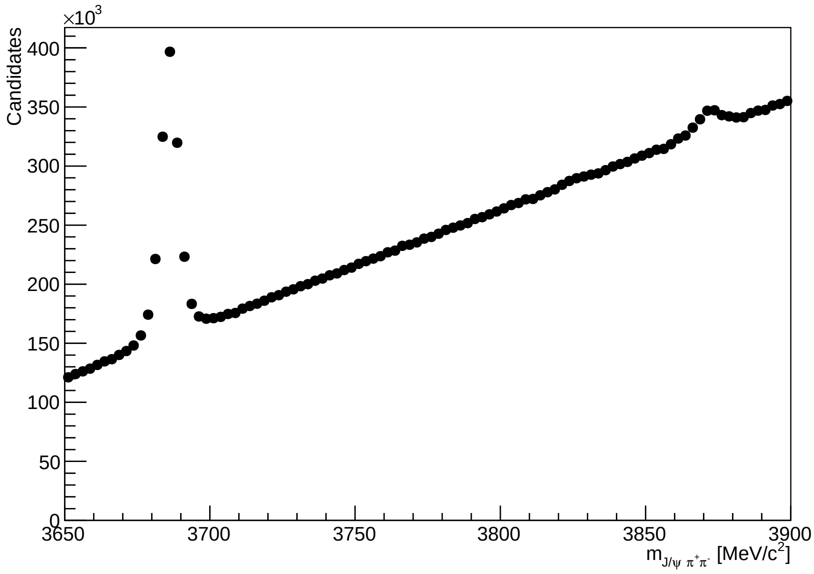

FIGURE 2.3: Plot of the corrected mass of all the reconstructed candidates possibly decaying into $J/\psi\pi^+\pi^-$ that satisfy the conditions of the stripping/reconstruction procedure but zoomed in on area of interest.

Further offline candidate Selection

After this stripping procedure we must further cut the data. Based on specific tests we optimised the data for further analysis. First of all, we are interested in the $\psi(2S)$ and $X(3872)$. So we will focus on the mass interval containing these and cut the rest: $3650 < m_{J/\psi\pi^+\pi^-} < 3900$ (Fig. 2.3). However, our primary focus is the $X(3872)$ and for low p_T the $X(3872)$ is not visible. So we searched for the lower bound above which the $X(3872)$ is seen and applied this cut. In Fig. 2.4 plots of the corrected mass in bins of p_T are shown. Based on these plots we chose $p_\mathrm{T} > 5000\,\mathrm{MeV}/c$ as a good cut.

The next step is optimising the candidate selection. A common indicator in determining this is the precision on the yield

$$PY = \frac{S}{\sqrt{S+B}}, \tag{2.1}$$

where S is the signal for $X(3872)$ and B is the signal for the background in the same region. This precision is the result of error propagation: if $N = S + B$ is the total number of events in the region around $X(3872)$, then at large S and B, Poisson statistics tend to Gaussian. So the statistical uncertainty on N is $\sqrt{N}$. Assuming you know B from a fit to large sidebands, you get $S = N - B$ and the uncertainty on S is $\sqrt{N}$. The cross-section on $X(3872)$ is proportional to S and its error to $\sqrt{N}$. So to get the most precise cross-section measurement we want to minimise $\frac{\sqrt{S+B}}{S}$, thus maximise $\frac{S}{\sqrt{S+B}}$.

For calculating these signals we performed a mass fit for different cuts to determine which cut returns the highest PY. The model we used for these fits is the sum of the three components: $X(3872)$, $\psi(2S)$ and background, respectively g_X, g_ψ and g_B, for which we used a probability density function (PDF) consisting of two Gaussian functions for the $\psi(2S)$(eq. 2.2), a single Gaussian function for $X(3872)$ (eq. (2.3)) , and where we used a second order *Chebychev polynomial* of the first kind to

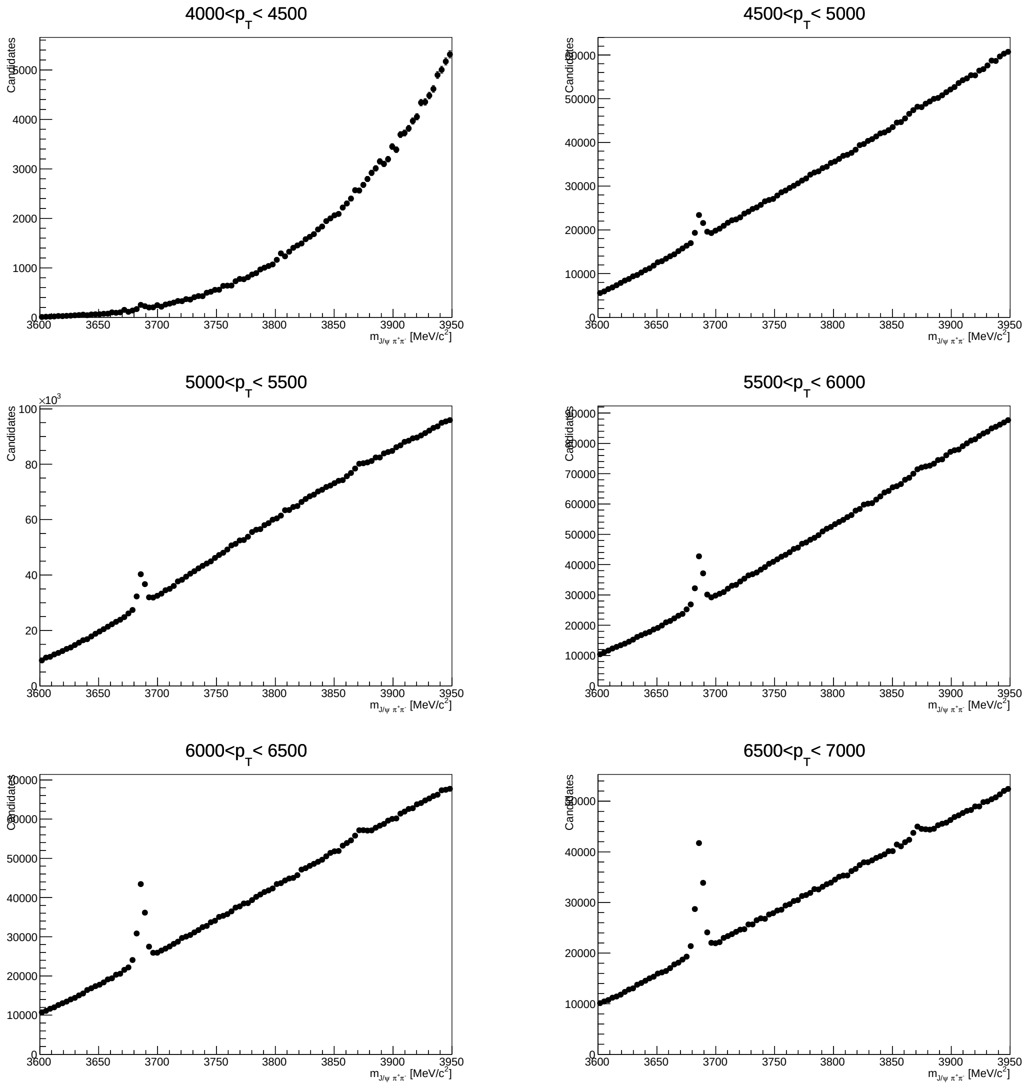

FIGURE 2.4: Plot of $m_{J/\psi\,\pi^+\pi^+}$ in bins of p_T

describe the background (eq. (2.4)).

$$g_\psi(m;\mu_\psi,\sigma_1,\sigma_2,\gamma) = \frac{\gamma}{\sqrt{2\pi}\sigma_1}e^{-\frac{(m-\mu_\psi)^2}{2\sigma_1^2}} + \frac{1-\gamma}{\sqrt{2\pi}\sigma_2}e^{-\frac{(m-\mu_\psi)^2}{2\sigma_2^2}} \tag{2.2}$$

$$g_X(m;\mu_X,\sigma_X) = \frac{1}{\sqrt{2\pi}\sigma_X}e^{-\frac{(m-\mu_X)^2}{2\sigma_X^2}} \tag{2.3}$$

$$g_B(m;c_1,c_2) = c_2(2m^2-1) + c_1 m + 1 \tag{2.4}$$

Where γ is the fraction of one Gaussian to the other, σ is the width of that Gaussian and μ is the mean, thus the theoretical mass of the particle. The choice for a double Gaussian is based on the fact that as we will see in the proceeding part that for calculating a consistent background signal in the region around $X(3872)$ for this optimisation it is important that the signal is symmetric (2.7). When assembling the complete model we will introduce some asymmetries (e.g. due to radiative effects) for a more complete model. However at this stage, i.e. determining the maximum of PY for different cuts, the importance of these asymmetries is negligible. The following function is then fitted to the corrected mass

$$G = n_X g_X + n_\psi g_\psi + n_B g_B, \tag{2.5}$$

where n_i is the yield of the specific component.

After this fit we do not use the yield of $X(3872)$ for S but we extrapolate the signal of $X(3872)$ from the signal for $\psi(2S)$ by multiplying it with the mean production ratio of $X(3872)$ to $\psi(2S)$: $R_{X(3872)/\psi(2S)}$, which is set to 0.15 from previous measurements [6]. A graphical representation of S is given in Fig. 2.6a (blue). Furthermore to give a consistent approach to the region around $X(3872)$, we solve (2.7) for x. Here we account for 99.7% of the signal. Then we use the same length of the determined interval but then centred around μ_X as integration interval for the calculation of the background (2.8). This way we get the total background surrounding X(3872). A graphical representation of B is given in Fig. 2.6a (magenta)

$$S = 0.997\, n_\psi R_{X(3872)/\psi(2S)} \tag{2.6}$$

$$2 \times \int_{\mu_\psi}^{\mu_\psi + x} g_{\psi(2S)}\, dm = 0.997 \tag{2.7}$$

$$B = \int_{\mu_X - x}^{\mu_X + x} g_B\, dm \quad . \tag{2.8}$$

Firstly, we wanted to optimise the pion PID cut. For obvious reasons we want the probability of a particle identified as a pion in fact being a pion to be as high as possible. However, by making this cut too high we lose too much statistics. So we made a fit in $m_{J/\psi\pi^+\pi^-}$ for different values of i when $P[\pi^+] > i$ and $P[\pi^-] > i$. A plot of the distribution of $P[\pi]$ can be seen in Fig. 2.5b. We then calculated PY for each i and plotted this precision yield PY as a function of i (see Fig. 2.6b). We found that the optimal cut is for which $i = 0.55$. Thus when $P[\pi^+] > 0.55$ and $P[\pi^-] > 0.55$.

Then we started looking at the mass window for the J/ψ. In the distribution of $m_{\mu^+\mu^-}$ (Fig. 2.5a) it can been seen that the data doesn't vanish when we look further from the known mass of J/ψ (3097 MeV/c^2). This indicates that there to is an amount of background in there. So it is preferred to cut away all data outside a certain window centred at $m_{\mu^+\mu^-} = 3097\,\mathrm{MeV}/c^2$. Again we have a trade-off in amount of background versus amount of signal that we cut. So to find the optimal window we again calculated PY for increasing j, where $|m_{J/\psi} - 3097| < j$. We then plotted the PY as a function of j. The results are shown in Fig. 2.6c . Here the optimal cut is $|m_{J/\psi} - 3097| < 37\,\mathrm{MeV}/c^2$.

Finally, we did the same for p_{T_π}. However this time it is not that obvious in to what side ($<$ or $>$) the cut should be. So we approached it in two different ways. First, we applied the cut $p_{T_\pi} > k$, for increasing k. Secondly $p_{T_\pi} > k$, for decreasing k. The results are shown in the figures 2.6d and 2.6e. We can see that the optimal cut is no cut at all.

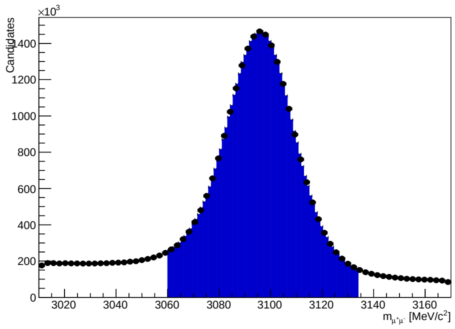

(A) Distribution of the mass for reconstructed J/ψ. In the blue area are the candidates for which $|m_{J/\psi} - 3097| < 37\,\mathrm{MeV}/c^2$.

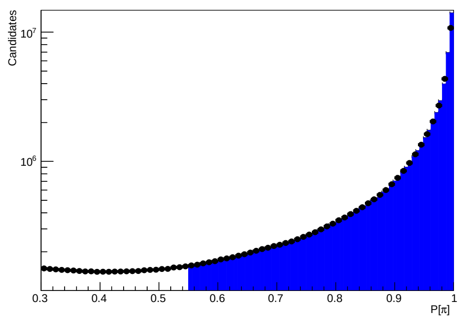

(B) The distrubitution of the pionPID. In blue are the candidates for which $P[\pi] > 0.55$.

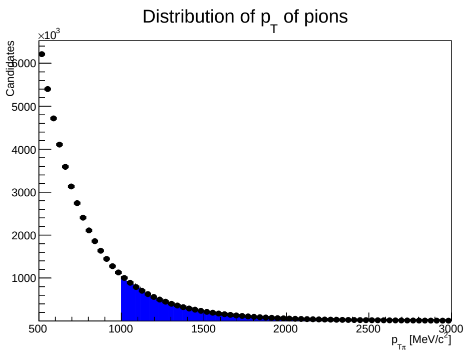

(C) Distribution of $p_{\mathrm{T}\pi}$. In blue are the candidates for which $p_{\mathrm{T}\pi} > 1000\,\mathrm{MeV}/c$

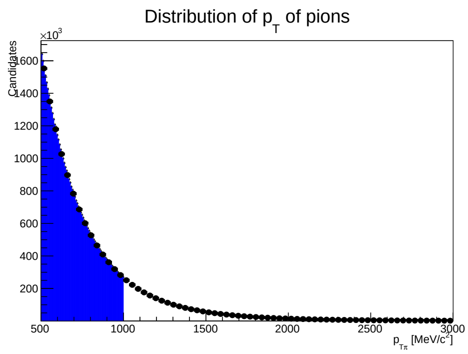

(D) Distribution of $p_{\mathrm{T}\pi}$. In blue are the candidates for which $500 < p_{\mathrm{T}\pi} < 1000\,\mathrm{MeV}/c$

FIGURE 2.5

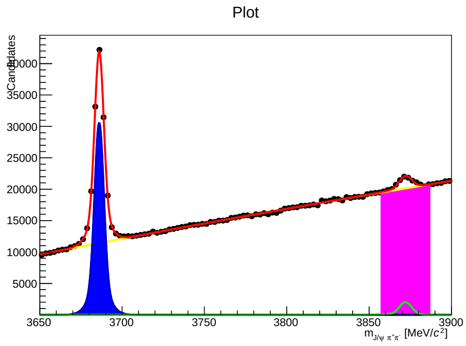

(A)

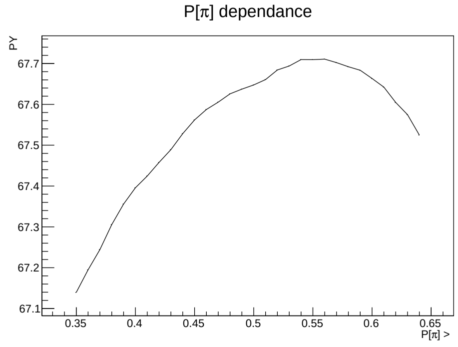

(B)

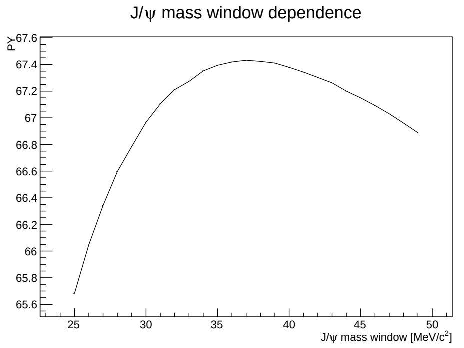

(C)

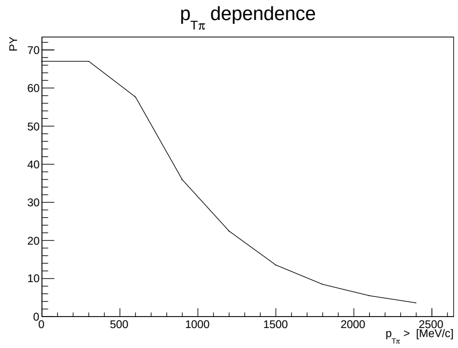

(D)

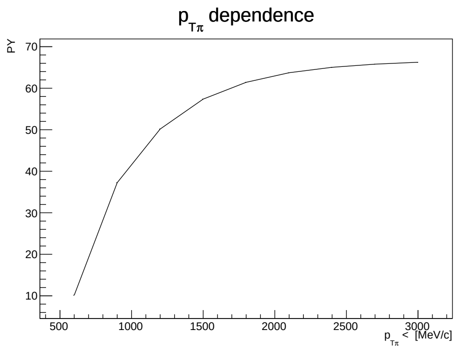

(E)

FIGURE 2.6: Plots concerning the precision yield. Fig. 2.6a shows the highlighted areas representing S (blue) and B (magenta). Fig. 2.6b shows the dependance of the precision yield on i for $P[\pi] > i$. Fig. 2.6c shows the dependance of the the precision yield on j for $|m_{J/\psi} - 3097| < k$. Fig. 2.6d and 2.6e show the dependance of the precision yield on l and k for respectively $p_{T\pi} > l$ and $p_{T\pi} < k$

3 The model

Now that the data is ready for our analysis, we shall proceed to build the two-dimensional PDF modeling the data best. When defining the model, each component of the signal will be a product of its mass part and pseudo-proper time part. However, an important thing to take into account when modeling the background is a possible correlation between these two observables. Which indeed there happens to be as we will see.

3.1 Mass

As mentioned before the component for the background is modelled with a second order *Chebyshev polyonomial* of the first kind. Now to check if there exists a correlation we fitted the mass shape for several bins of t_z (Fig. 3.2 and 3.3). We then plotted the parameters of the Chebychev polynomial describing the background versus t_z (Fig. 3.1a and 3.1b). As you can see the coefficients flatten out after approximately $t_z = 0.05$, especially the c_1 which is most dominant for the shape. This indicates a semi-correlation, i.e. that the prompt and and non prompt background component have different mass shapes. But once separated they do not change with t_z. Thus, when assembling the full 2D model we must split the background in to two separate parts. Both parts of the background component will have a Chebychev polynomial (2.4) describing the mass, but they will have slightly different values for their parameters.

For the $\psi(2S)$, we will now replace one of the Gaussian shapes by a *Crystal Ball* shape. Which is defined as

$$g_{CB}(m;\mu,\sigma,\alpha,n) = \begin{cases} \frac{\left(\frac{n}{|\beta|}\right)^n e^{-\frac{1}{2}\beta^2}}{\left(\frac{n}{|\beta|}-|\beta|-\frac{m-\mu}{\sigma}\right)^n} & \frac{m-\mu}{\sigma} < -|\alpha| \\ e^{-\frac{1}{2}\left(\frac{m-\mu}{\sigma}\right)^2} & \frac{m-\mu}{\sigma} > -|\alpha|. \end{cases} \tag{3.1}$$

This shape combines a Gaussian core with one tail to the left. The tail described with this Crystal Ball shape are introduced to model radiative effects, which lead to more candidates with lower corrected mass.

The mass shape for the $X(3872)$ will remain the same: a single Gaussian. Theoretically it should also have a tail due to radiative effects. However, because this signal is so week, adding a Crystal Ball does not improve the the fit whatsoever. Instead it only adds extra parameters, increasing the complexity of the fit. So we arrive at our final PDF's modeling the corrected mass of our components

$$
\begin{aligned}
g_\psi(m;\mu_\psi,\sigma_{\psi 1},\sigma_{\psi 2},\gamma) &= \frac{\gamma}{\sqrt{2\pi}\sigma_{\psi 1}} e^{-\frac{(m-\mu_\psi)^2}{2\sigma_{\psi 1}^2}} + (1-\gamma) g_{CB}(m;\mu_\psi,\sigma_{\psi 2},\alpha,n=1) \\
g_X(m;\mu_X,\sigma_X) &= \frac{1}{\sqrt{2\pi}\sigma_X} e^{-\frac{(m-\mu_X)^2}{2\sigma_X^2}} \\
g_{Bp}(m;c_{1p},c_{2p}) &= c_{2p}(2m^2-1) + c_{1p}m + 1 \\
g_{Bnp}(m;c_{1np},c_{2np}) &= c_{2np}(2m^2-1) + c_{1np}m + 1
\end{aligned}
\tag{3.2}
$$

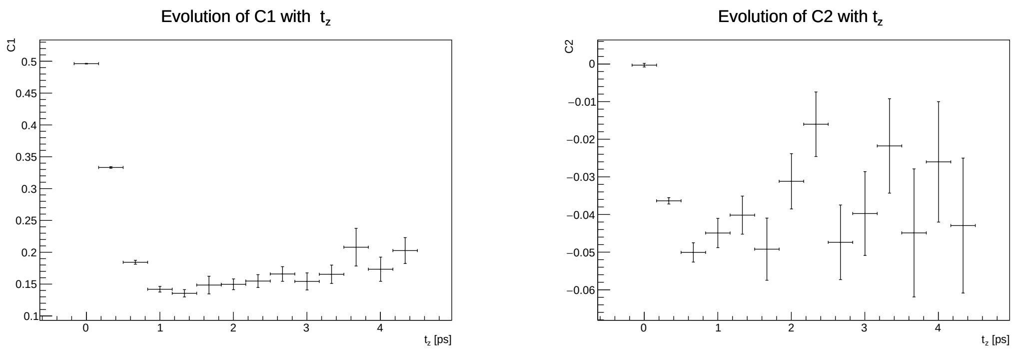

(A) (B)

FIGURE 3.1: The evolution with t_z of the first (left) and second (right) parameter of the Chebychev polynomial describing the background.

3.2 Pseudo proper time

For determining the PDF's for the pseudo-proper time we must first define a resolution model. The difference with the mass measurement is that lifetime measurements are much more precise. We therefore model the resolution by a Gaussian (equation (3.3)). Then the PDF for a component in the pseudo-proper time will be a convolution of the resolution and the theoretical function describing the physics. By doing this the resolution of the detector will be taken into account for each point along the PDF.

$$
f_{resolution}(t_z;\mu,\sigma) = \frac{e^{-\frac{(t_z-\mu)^2}{2\sigma^2}}}{\sqrt{2\pi}\sigma}
\tag{3.3}
$$

As mentioned before the t_z is used to make a distinction between the particles that are created promptly (upon collision) and those that come from a b hadron. Thus we can split the signal into two parts for each component. For $\psi(2S)$ and $X(3872)$ they thus consist of delta peak for the prompt and an exponential modeling the non prompt part. When it is convoluted with the resolution model this delta peak will of course be "smeared" (equations (3.4) and (3.5)).

$$
f_\psi(t_z;\tau_\psi,\beta_\psi) = \left[(1-\beta_\psi)\delta(t_z) + \Theta(t_z)\frac{\beta_\psi}{\tau_\psi}e^{\frac{-t_z}{\tau_\psi}}\right] * f_{resolution}
\tag{3.4}
$$

$$
f_X(t_z;\tau_X,\beta_X) = \left[(1-\beta_X)\delta(t_z) + \Theta(t_z)\frac{\beta_X}{\tau_X}e^{\frac{-t_z}{\tau_X}}\right] * f_{resolution}
\tag{3.5}
$$

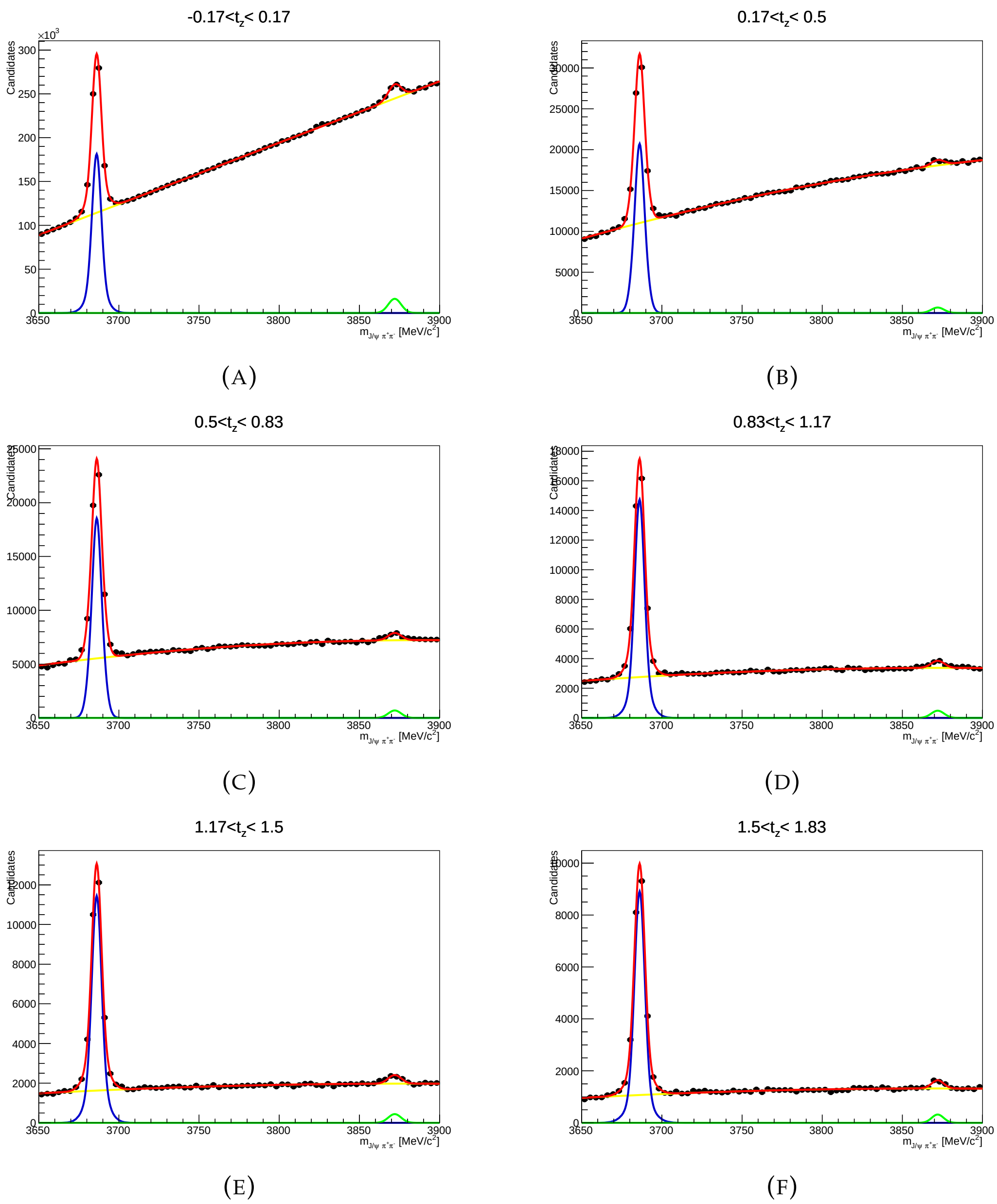

(A) (B) (C) (D) (E) (F)

FIGURE 3.2: The mass fits in bins of t_z. These fitresults were used to make the plots in Fig. 3.1.

Where τ_ψ and τ_X are the pseudo-lifetimes of respectively $\psi(2S)$ and $X(3872)$, and β_ψ and β_X are their fractions for the of prompt and non prompt part. Furthermore, $\Theta(t_z)$ is the heavyside step function defined by

$$\Theta(t_z) = \begin{cases} 0 & t_z < 0 \\ 1 & t_z > 0. \end{cases} \tag{3.6}$$

This is introduced to ensure the exponential tail only lives on positive lifetime, because a negative lifetime is unphysical. However, there are events for which $t_z < 0$. We model these as part of the resolution and also in the prompt background PDF. For the background we define the prompt and non prompt part separately because they will be multiplied by different mass-PDF's. We use two exponentials for the non prompt part. For the prompt part we use a exponential mirrored at $t_z = 0$ and

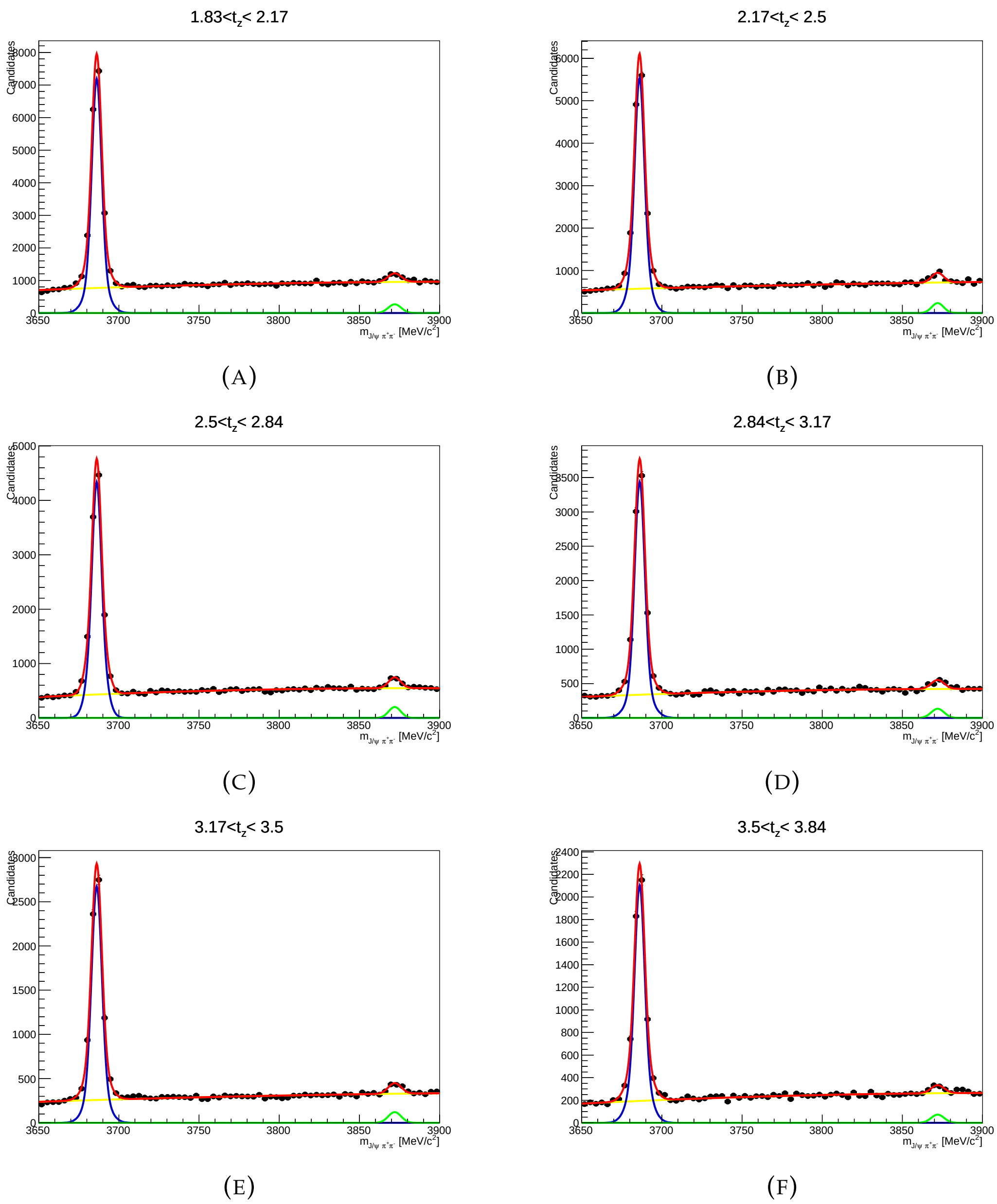

FIGURE 3.3: The mass fits in bins of t_z. These fit results were used to make the plots in Fig. 3.1.

also a delta peak (see Fig. 3.4).

$$f_{Bnp} = \left[\Theta(t_z)\left(\frac{\beta_1}{\tau_1}e^{\frac{-t_z}{\tau_1}} + \frac{1-\beta_1}{\tau_2}e^{\frac{-t_z}{\tau_2}}\right)\right] * f_{resolution} \tag{3.7}$$

$$f_{Bp} = \left[(1-\beta_2)\delta(t_z) + \frac{\beta_2}{\tau_3}e^{\frac{|-t_z|}{\tau_3}}\right] * f_{resolution} \tag{3.8}$$

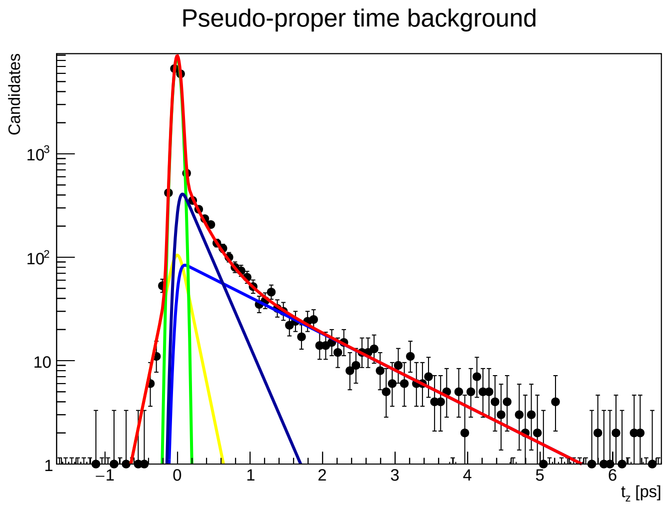

FIGURE 3.4: An example of a t_z fit of a bin in the background ($2.5 < y < 3$, $7 < p_T < 8\,\mathrm{GeV}/c$ and $3760 < t_z < 3770\,\mathrm{MeV}/c^2$). Here you can see the different components of the model describing the t_z component of the background. The resolution (green), the two decay tails (two shades of blue) and the the prompt double sided component (yellow).

3.3 2D model

The total model is obtained by multiplying the PDF for the mass with the PDF for the pseudo-proper time for each component separately and then adding these components with their yield as a prefactor (3.9).

$$F = n_X(g_X \times f_X) + n_\psi(g_\psi \times f_\psi) + n_{Bp}(g_{Bp} \times f_{Bp}) + n_{Bnp}(g_{Bnp} \times f_{Bnp}) \tag{3.9}$$

4 Results

Unfortunately there was no Monte Carlo simulation available for the $X(3872)$ production at $\sqrt{s} = 13$ TeV. Therefore we were not able to perform any efficiency corrections. However even though we expect the efficiency to be slightly different for $X(3872)$ and $\psi(2S)$, the ratio of efficiencies would not vary a lot with p_{T} and y.

4.1 Binned 2D fit

The model (3.9) has been fitted to the data in ten bins of p_{T} (5-15 GeV/c) and five bins of y (2-4.5). An example of the two-dimensional fit is shown in Fig. 4.1. The results of the fitted parameters are shown in appendix A. In Fig. 4.2-4.4 the production ratio between $X(3872)$ and $\psi(2S)$ is plotted as a function of p_{T} for the five bins of y. These plots are shown for the total, prompt and non prompt production cross sections separately. In Fig. 4.5 the ratio of the prompt production ratio versus the non prompt production ratio is shown as function of p_{T} in the five bins of y. In addition to this we also plotted the prompt, non prompt and ratios between these two for the 5 bins of y and ten bins of p_{T} separately (Fig. 4.6). Thus, in the first case we integrate over p_{T} and plot the ratio's and ratio of ratio's as a function of y. In the second case vice versa.

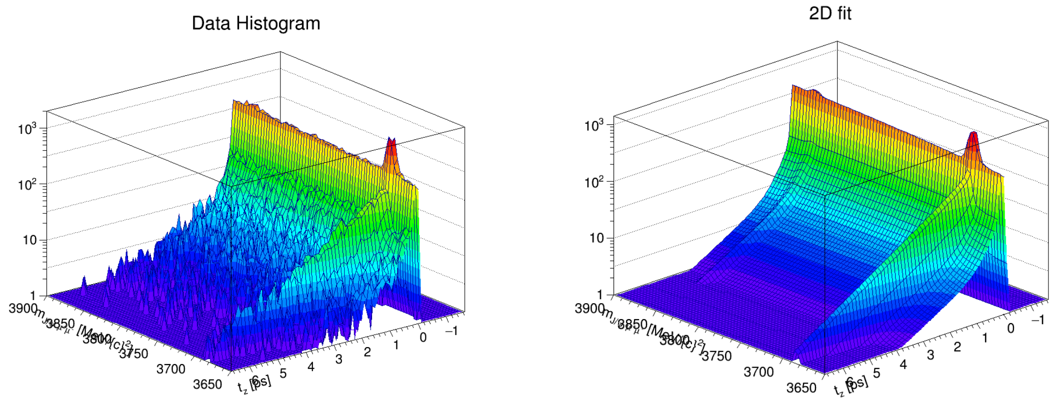

FIGURE 4.1: (left) A two dimensional plot of the data in the bin ($2.5 < y < 3$, $7 < p_{\mathrm{T}} < 8\,\mathrm{GeV}/c$). (right) The two dimensional fit in the same bin.

On all these plots we performed a polynomial 0 fit to check the flatness of the ratio's. These are displayed in the same plots with the corresponding statistics.

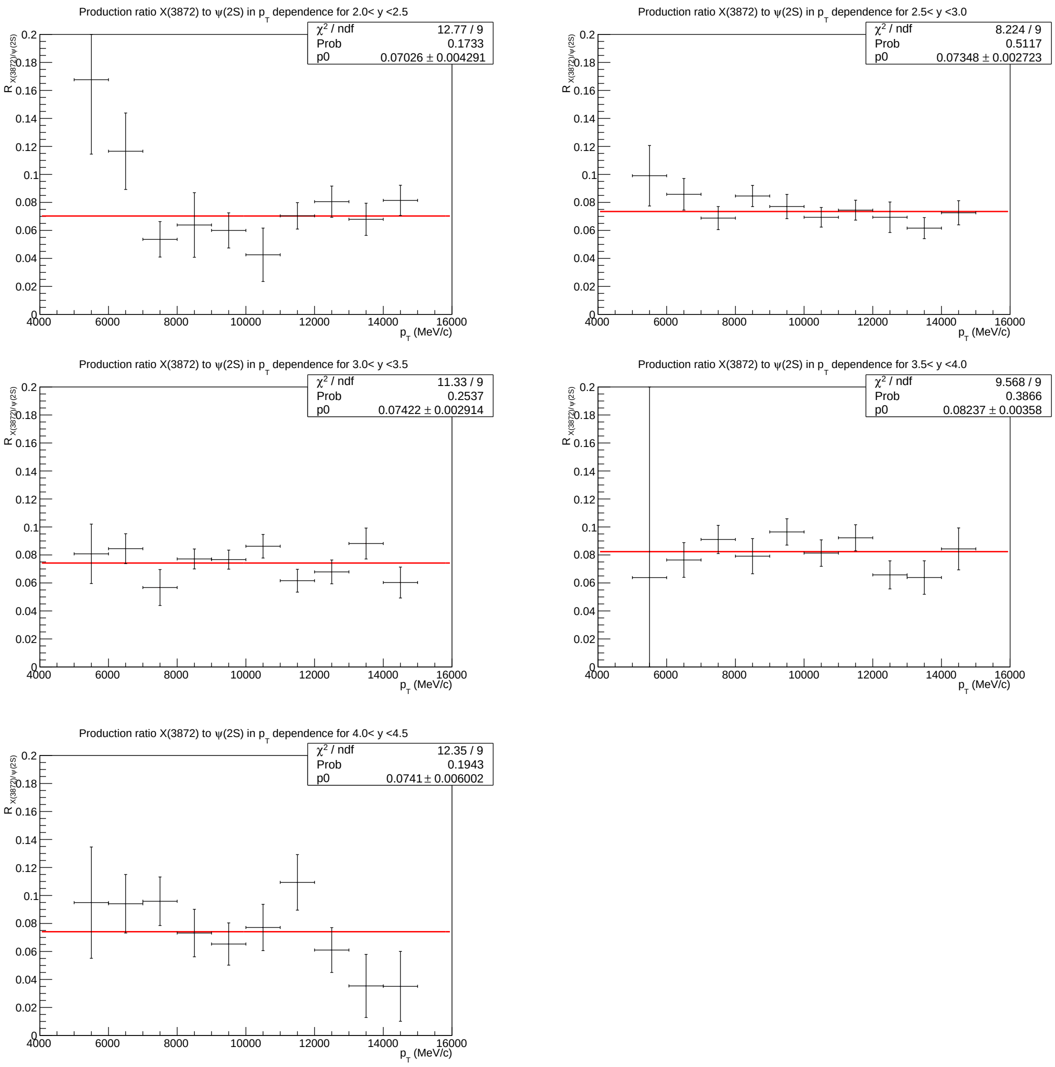

FIGURE 4.2: Plots of the total production ratio $R_{X(3872)/\psi(2S)}$ as a function of p_{T} in bins of y. They are fitted with a zero polynomial. The results are shown in the top right corner with χ^2 per degrees of freedom, probability and central value.

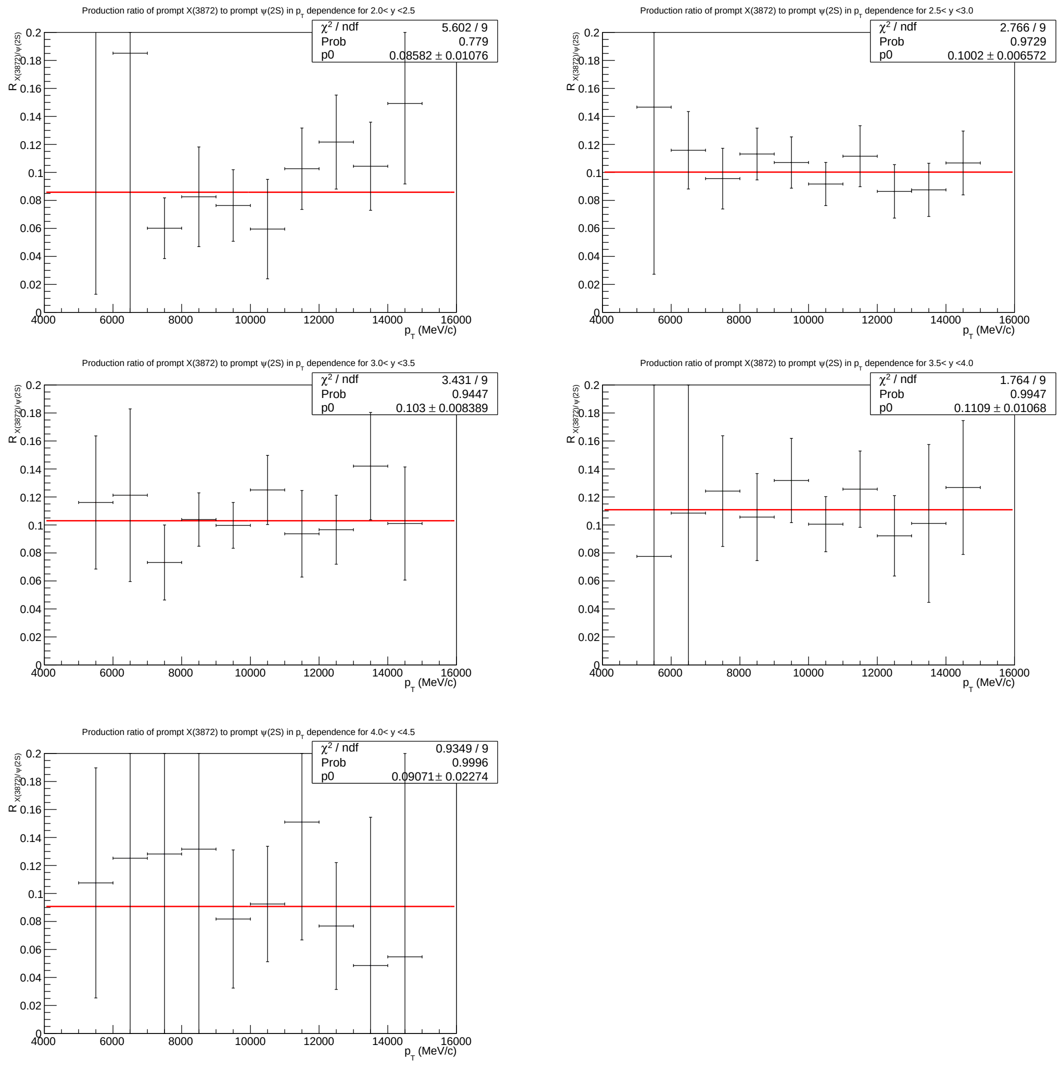

FIGURE 4.3: Plots of the prompt production ratio $R_{X(3872)/\psi(2S)}$ as a function of p_{T} in bins of y. They are fitted with a zero polynomial. The results are shown in the top right corner with χ^2 per degrees of freedom, probability and central value.

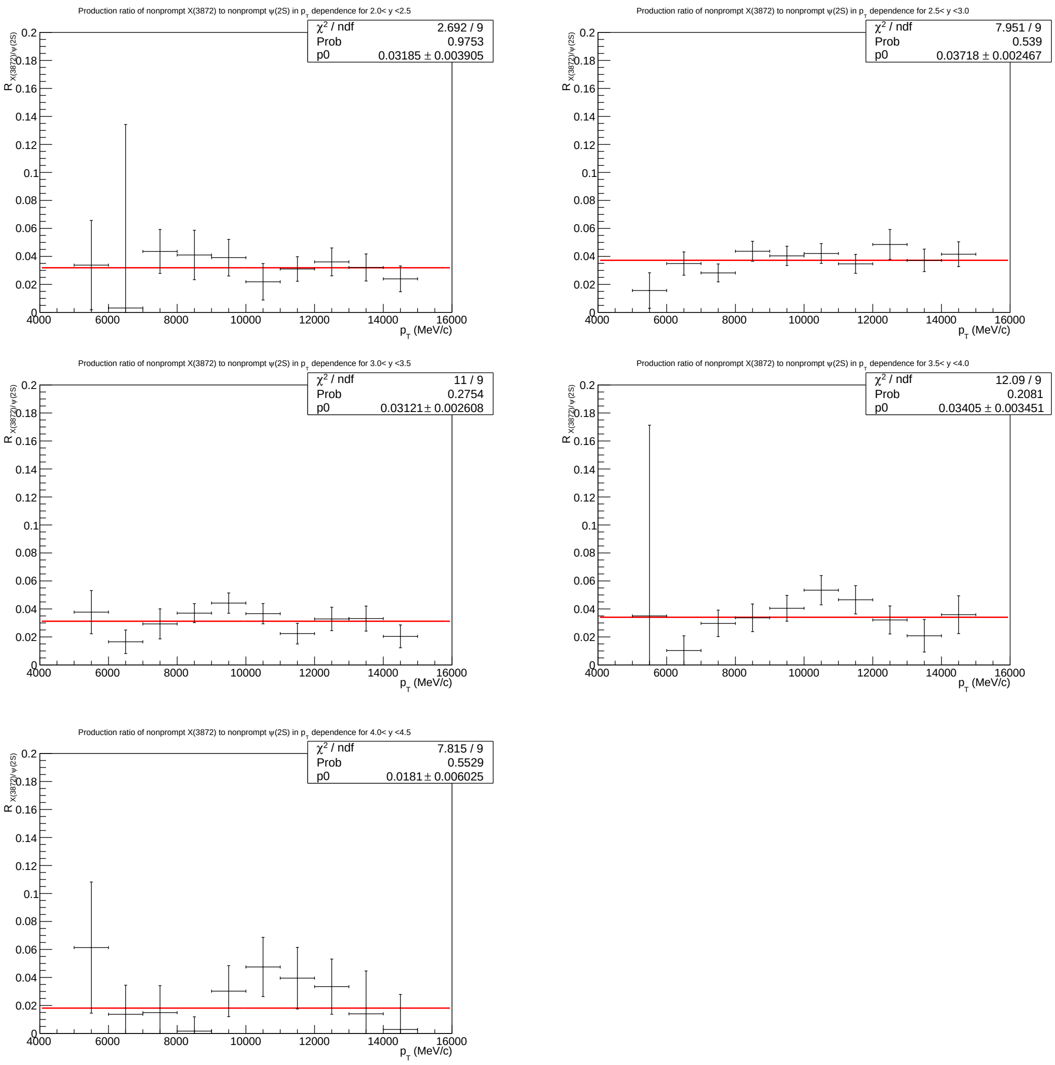

FIGURE 4.4: Plots of the non prompt production ratio $R_{X(3872)/\psi(2S)}$ as a function of p_{T} in bins of y. They are fitted with a zero polynomial. The results are shown in the top right corner with χ^2 per degrees of freedom, probability and central value.

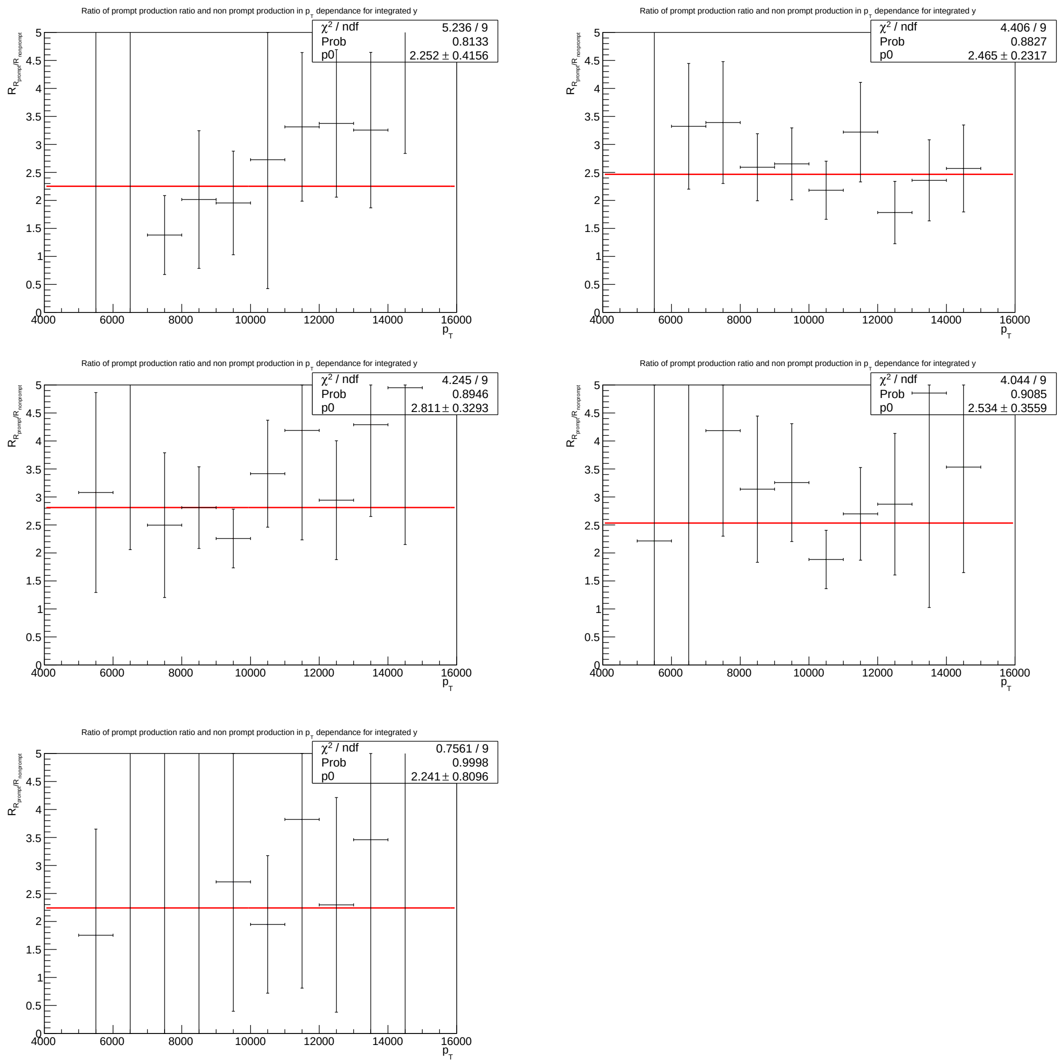

FIGURE 4.5: Plots of the ratio of the prompt production ratio (Fig. 4.3) versus the non prompt production ratio (4.4) as a funciton of p_{T} in bins of y. They are fitted with a zero polynomial. The results are shown in the top right corner with χ^2 per degrees of freedom, probability and central value.

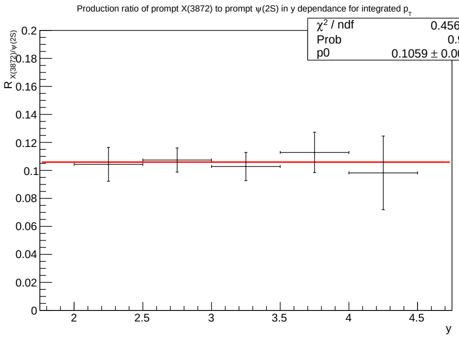

(A)

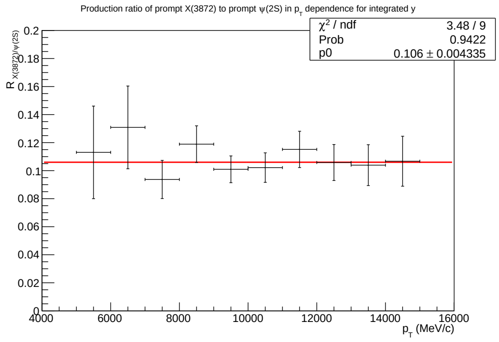

(B)

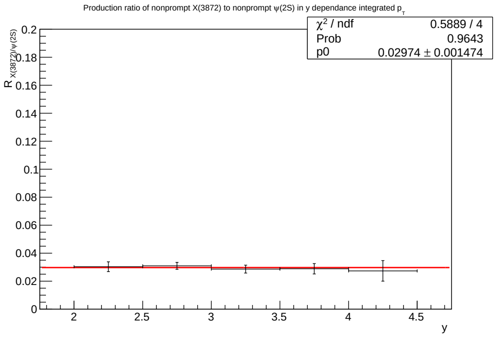

(C)

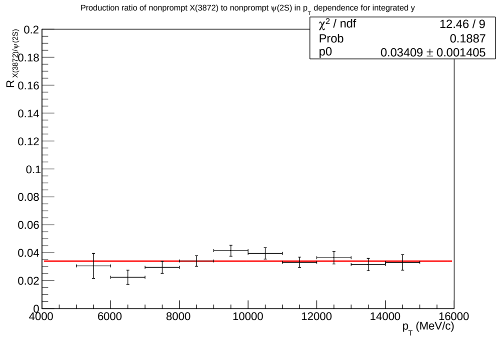

(D)

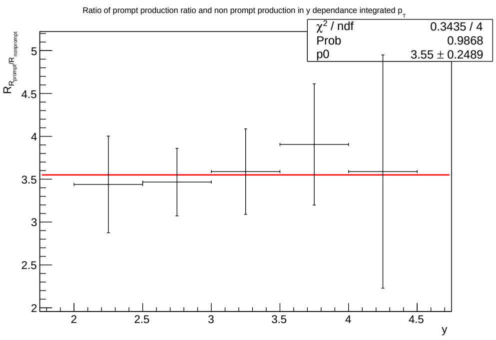

(E)

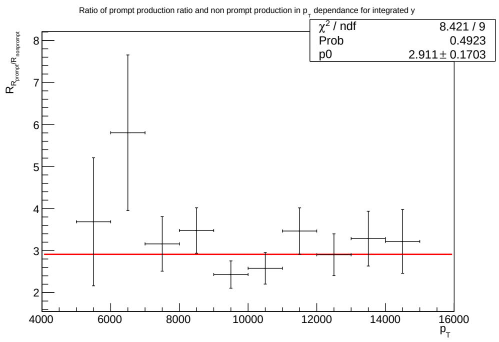

(F)

FIGURE 4.6: (left) From top to bottom: Plots of the prompt production ratio, non prompt production ratio and ratio between these two as a function of p_T for integrated y. (right) From top to bottom: Plots of the prompt production ratio, non prompt production ratio and ratio between these two as a function of y for integrated p_T. They are fitted with a zero polynomial (flat line). The results are shown in the top right corner with χ^2 per degrees of freedom, probability and central value.

4.2 Non prompt $X(3872)$

In this section we take a closer look at the non prompt production of $X(3872)$. For this part of the analysis we apply an additional cut to the data, namely, $m_{\pi^+\pi^-} > 600\,\text{MeV}/c^2$. In Fig. 4.7a the distribution of $m_{\pi^+\pi^-}$ is shown with the applied cut. The goal of this cut is to increase significance of the $X(3872)$ signal by cutting away more background but maintaining the signal for $X(3872)$. The choice of 600 MeV/c^2 is based on the fact that this is the minimum mass required from the $m_{\pi^+\pi^-}$ to reach the mass of $X(3872)$ when added to that of J/ψ. Consequently the signal for $\psi(2S)$ is cut away as well (as can be seen in Fig. 4.7b). However, we no longer look at the $\psi(2S)$ for this part of the analysis. Thus there is no conflict. As we are only interested in the $X(3872)$ we further narrow our mass interval to $3850 < m_{J/\psi\pi^+\pi^-} < 3900\,\mathrm{MeV}/c^2$. We then performed a mass fit to these two separate curves and compared the yield of $X(3872)$ for both fits. The yield for $X(3872)$ stayed approximately the same (before vs. after : 4088 ± 196 vs. 4082 ± 207). And the background decreased by a factor 3. Thus achieving the goal. We then use the data to perform a single two dimensional fit. The fit is done on the total pseudo proper time spectrum, but after fitting we will focus on the non prompt part ($t_z > 0.5\,\mathrm{ps}$). A plot of the data for $t_z > 0.5\,\mathrm{ps}$, $3850 < m_{J/\psi\pi^+\pi^-} < 3900\,\mathrm{MeV}/c^2$ and the applied cut on the di-pion mass can be seen in Fig. 4.7d.

This two dimensional fit is done using almost the same model as before (3.9), but with some adjustments. First of all, as we cut away the signal for $\psi(2S)$ we will not need this component in our model anymore. So we leave it out. Then we add an additional exponential to our $X(3872)$ component and fix the parameter $\tau_{B_c^+} = 0.509\,\mathrm{ps}$ [11]. To further simplify the model a bit we do not separately use a different mass shape for the prompt and non prompt background component. This is justified by the fact that as the the mass interval is considerably shorter the shape does not change significantly with t_z.

$$f_{X'}(t_z;\tau_X,\beta_X,\tau_{B_c^+},\beta_{B_c^+}) = \left[(1-\beta_X-\beta_{B_c^+})\delta(t_z) + \Theta(t_z)\frac{\beta_X}{\tau_X}e^{\frac{-t_z}{\tau_X}} + \Theta(t_z)\frac{\beta_{B_c^+}}{\tau_{B_c^+}}e^{\frac{-t_z}{\tau_{B_c^+}}}\right] * f_{resolution} \tag{4.1}$$

$$F = n_X(g_X \times f_{X'}) + n_B(g_B \times (\beta_p f_{Bp} + (1-\beta_p) f_{Bnp})) \tag{4.2}$$

Then the fit result of the additional free parameter, $\beta_{B_c^+}$, is the number we're interested in. As discussed in section 1.1 ATLAS found a large fraction of $X(3872)$ from B_c^+ decays: $25 \pm 12 \pm 2 \pm 5$ %. This number would in our case represent

$$\Gamma = \frac{\sigma(B_c^+ \to X(3872))}{\sigma(X \to X(3872))} = \frac{\beta_{B_c^+}}{\beta_X + \beta_{B_c^+}}. \tag{4.3}$$

We performed the fit using the adjusted model (4.2). A plot of the fit is shown in Fig. 4.7e with the associated pulls in Fig. 4.7f. The fit results are presented in table 4.1. In addition we performed a cross-check fit on $\psi(2S)$ to check if the main life time component we measure for the $X(3872)$ and $\psi(2S)$ are in fact originating from b- hadrons. This was done in equivalent manner. We added a second exponential with fixed lifetime $\tau_{B_c^+} = 0.509\,\mathrm{ps}$ and focused on the the mass $3660 < m_{J/\psi\pi^+\pi^-} < 3710\,\mathrm{MeV}/c^2$. We left out the di-pion mass cut for obvious reasons. The plots corresponding to this cross-check fit are displayed in Fig. 4.9. The fit results are shown in Table 4.1.

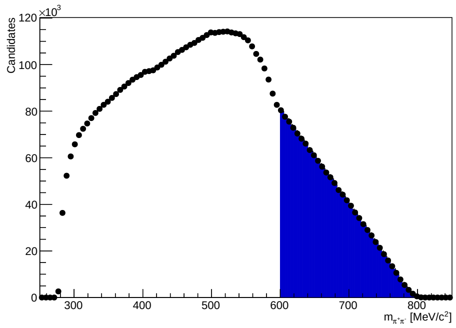

(A) Plot of the mass distribution of $\pi^+\pi^-$ with $m_{\pi^+\pi^-} > 600\,\text{MeV}/c^2$ in blue.

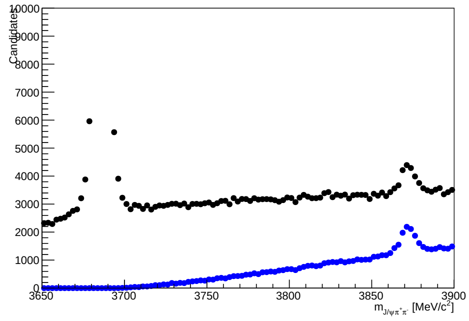

(B) Plot of the corrected mass in black for $t_z > 0.5$. Plot of the corrected mass for $t_z > 0.5$ with applied cut $m_{\pi^+\pi^-} > 600\,\text{MeV}/c^2$ in blue.

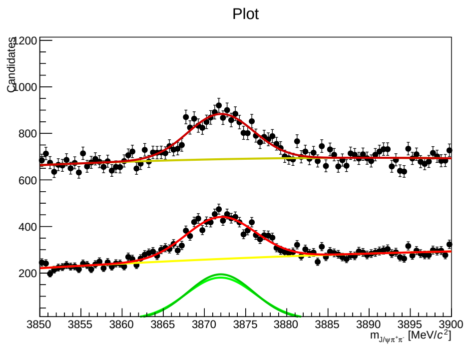

(C) A fit of the corrected mass for both curves from Fig. 4.7b.

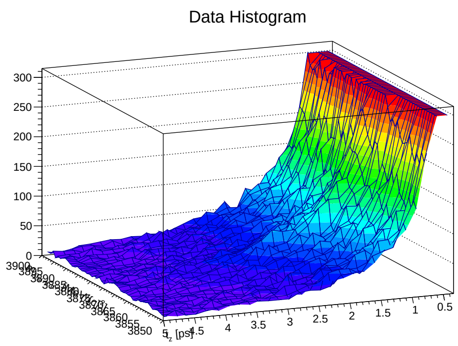

(D) Two dimensional plot of the data with applied cut $m_{\pi^+\pi^-} > 600\,\text{MeV}/c^2$ and in the mass range $3850 < m_{J/\psi\pi^+\pi^-} < 3900\,\text{MeV}/c^2$.

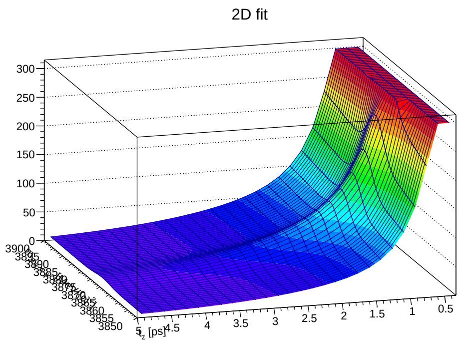

(E) The two dimensional fit of the data from Fig. 4.7d.

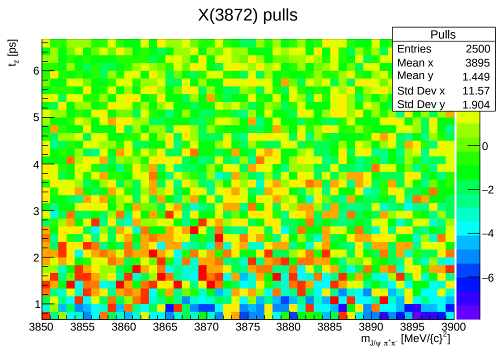

(F) The pulls belonging to the fit from Fig. 4.7e

FIGURE 4.7

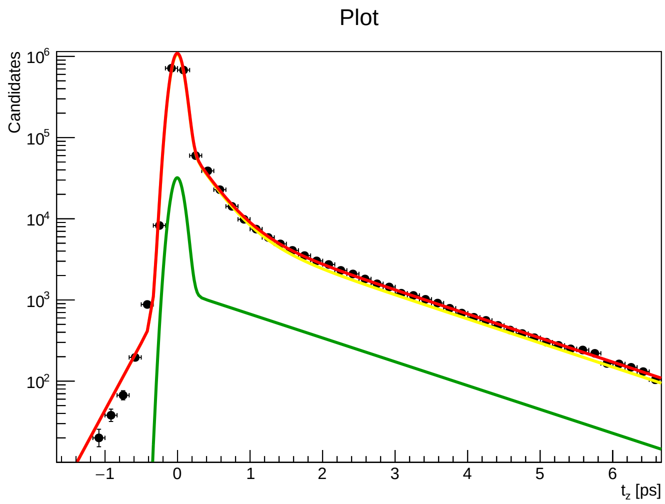

FIGURE 4.8: A plot of the fit of the of Fig. 4.7e integrated over the mass. The PDF for $X(3872)$ (green) and the background (yellow) are also plotted separately.

Parameters	Value ± Error	Parameters	Value ± Error
β_X	0.23± 0.006	β_ψ	0.42± 0.001
$\beta_{B_c^+}$	0.0± 0.003	$\beta_{B_c^+}$	0.0± 0.0
τ_X	1.48± 0.038	τ_ψ	1.46± 0.001
τ_1	1.47± 0.013	τ_1	1.63± 0.017
τ_2	0.3± 0.002	τ_2	0.5± 0.003
$n_X * 1000$	51.22± 1.035	$n_\psi * 1000$	612.46± 1.54
$n_B * 1000$	1548.34± 1.602	$n_B * 1000$	2009.38± 1.94
σ_{res}	0.08±0.0	σ_{res}	0.09±0.0
σ_X	4.0±0.035	$\sigma_{\psi 1}$	3.04±0.007
Corr(β_X,$\beta_{B_c^+}$)	-0.082	Corr(β_ψ,$\beta_{B_c^+}$)	-0.17
Γ	0.0±0.013	Γ	0.0±0.0

TABLE 4.1: (left) The fitted parameters belonging to the fit described in section 4.2. (right) The fitted parameters belonging to the cross-check fit for the $\psi(2S)$.

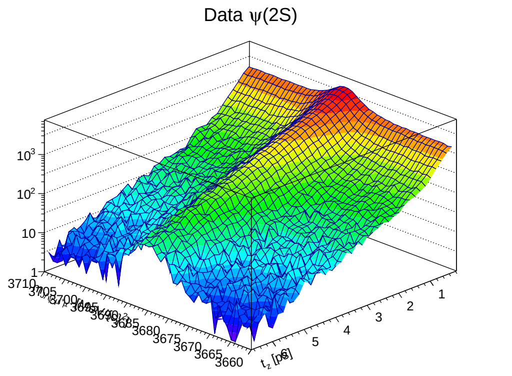

(A) Data plot from the cross-check fit of the $\psi(2S)$

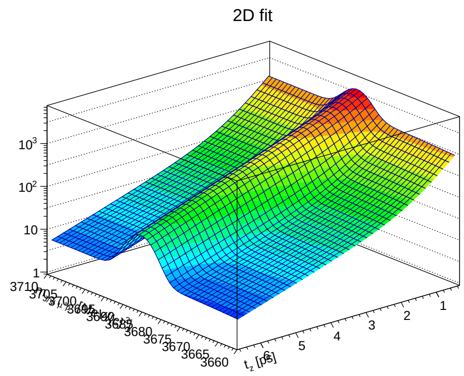

(B) The PDF plot from the cross-check fit of the $\psi(2S)$

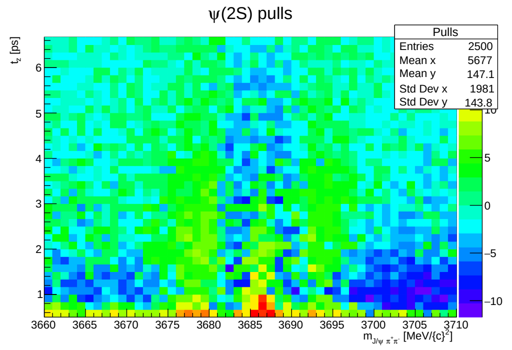

(C) The pulls from the cross-check fit of the $\psi(2S)$

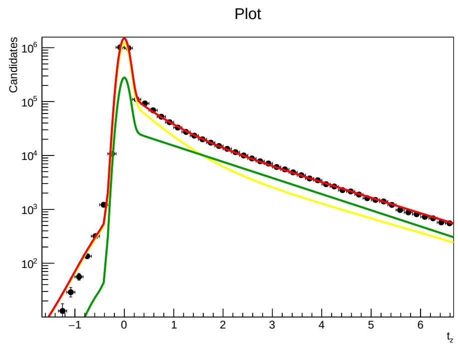

(D) A plot of Fig. 4.9a and 4.9b both integrated over mass.

FIGURE 4.9

5 Conclusion and Discussion

When we look at Fig. 4.2-4.6 we can see that all plots are flat within errors with high probabilities and an acceptable χ^2. Thus the ratio's are independent of y and p_{T}. This is an indication that the $X(3872)$ does not have a difference in behaviour with respect to $\psi(2S)$ when produced. Thus acting as evidence that $X(3872)$ is produced as a compact object. As discussed in Ref. [9], when $X(3872)$ would behave like a molecule, one would expect a deviation at lower p_{T}.

Furthermore when we look at the results in Table. 4.1 they tell us that the fraction of non prompt $X(3872)$ produced in B_c^+ decays is 0 with an uncertainty of 1.3%. This is, within uncertainty, more in line with what we would expect and contradicts the claim made by ATLAS. Also, for the main life times ($\tau_X = 1.48 \pm 0.038$ ps and $\tau_\psi = 1.46 \pm 0.001$ ps) are well in agreement with the measured lifetimes of the other b-hadrons, which average around 1.5 ps [11].

For future studies it would be useful to include an analysis with Monte Carlo simulation in order to calculate efficiencies. It would also be interesting to go to even lower p_{T} to see if the hard p_{T} spectrum still holds and test the model of $X(3872)$ being produced as a compact object even further. It is also expected that the absoluut production cross section of $\psi(2S)$ for $\sqrt{s} = 13$ TeV is to be measured in the near future. It would be interesting to extrapolate the absolute production cross section of $X(3872)$ from this.

A Parameters 2D fit

TABLE A.1: The parameters of the two-dimensional fit in m and t_z for different p_T bins in the rapidity bin $2.0 < y < 2.5$

Parameters	5-6	6-7	7-8	8-9	9-10
τ_ψ	1.53± 0.022	1.51± 0.014	1.46± 0.011	1.4± 0.009	1.41± 0.009
τ_1	0.4± 0.002	0.4± 0.002	0.38± 0.002	0.37± 0.002	0.36± 0.002
τ_2	1.7± 0.023	1.6± 0.016	1.63± 0.014	1.6± 0.012	1.58± 0.012
$n_X * 1000$	0.55± 0.174	0.77± 0.18	0.48± 0.113	0.63± 0.227	0.6± 0.126
$n_\psi * 1000$	3.31± 0.157	6.65± 0.197	9.01± 0.226	9.86± 0.228	10.04± 0.185
$n_{Bp} * 1000$	264.91± 0.605	251.48± 0.596	193.8± 0.526	138.85± 0.473	97.06± 0.39
$n_{Bnp} * 1000$	40.37± 0.318	49.51± 0.348	46.72± 0.321	39.98± 0.306	32.34± 0.262
β_X	0.07± 0.064	0.01± 0.424	0.32± 0.087	0.29± 0.068	0.29± 0.075
β_ψ	0.36± 0.017	0.38± 0.01	0.39± 0.008	0.45± 0.0	0.44± 0.007
σ_{res}	0.02±0.0	0.02±0.0	0.02±0.0	0.02±0.0	0.02±0.0
σ_X	4.0±1.187	4.0±0.179	2.5±0.266	3.69±1.072	4.0±1.348
$\sigma_{\psi 1}$	3.98±0.714	2.26±0.109	2.37±0.147	2.31±0.061	2.52±0.047
$\sigma_{\psi 2}$	2.5±0.143	4.59±0.241	4.26±0.395	4.73±0.258	5.71±0.345
γ	0.3±0.023	0.46±0.05	0.46±0.093	0.5±0.0	0.7±0.015
Parameters	10-11	11-12	12-13	13-14	14-15
τ_ψ	1.43± 0.009	1.47± 0.01	1.41± 0.01	1.44± 0.011	1.38± 0.011
τ_1	0.34± 0.002	0.33± 0.003	0.32± 0.004	0.29± 0.004	0.29± 0.005
τ_2	1.57± 0.012	1.49± 0.012	1.48± 0.012	1.51± 0.013	1.46± 0.014
$n_X * 1000$	0.39± 0.173	0.56± 0.075	0.51± 0.07	0.38± 0.063	0.39± 0.051
$n_\psi * 1000$	9.05± 0.142	7.99± 0.132	6.28± 0.107	5.54± 0.106	4.78± 0.11
$n_{Bp} * 1000$	66.76± 0.339	46.97± 0.271	33.45± 0.232	23.81± 0.205	17.56± 0.178
$n_{Bnp} * 1000$	25.28± 0.23	19.99± 0.204	15.53± 0.179	12.45± 0.167	9.39± 0.149
β_X	0.23± 0.091	0.2± 0.049	0.22± 0.051	0.24± 0.059	0.16± 0.057
β_ψ	0.45± 0.0	0.45± 0.0	0.48± 0.008	0.5± 0.009	0.54± 0.01
σ_{res}	0.02±0.0	0.02±0.0	0.02±0.0	0.02±0.0	0.02±0.0
σ_X	3.61±1.063	3.29±0.407	3.41±0.401	3.11±0.525	4.0±0.218
$\sigma_{\psi 1}$	3.96±0.146	4.09±0.163	5.0±0.275	4.73±0.447	2.36±0.217
$\sigma_{\psi 2}$	2.3±0.062	2.33±0.069	2.72±0.129	2.87±0.09	4.17±0.326
γ	0.5±0.0	0.5±0.0	0.3±0.328	0.3±0.026	0.37±0.103

TABLE A.2: The parameters of the two-dimensional fit in m and t_z for different p_T bins in the rapidity bin $2.5 < y < 3.0$

Parameters	5-6	6-7	7-8	8-9	9-10
τ_ψ	1.49± 0.009	1.53± 0.007	1.49± 0.006	1.5± 0.006	1.47± 0.006
τ_1	0.39± 0.001	0.4± 0.001	0.39± 0.001	0.37± 0.001	0.35± 0.001
τ_2	1.56± 0.008	1.7± 0.009	1.7± 0.008	1.61± 0.007	1.6± 0.008
$n_X * 1000$	1.84± 0.4	2.5± 0.327	2.22± 0.266	2.6± 0.231	2.05± 0.23
$n_\psi * 1000$	18.58± 0.327	29.09± 0.368	32.35± 0.352	30.7± 0.351	26.65± 0.311
$n_{Bp} * 1000$	1380.93± 1.378	990.54± 1.165	637.45± 0.945	399.64± 0.77	252.1± 0.627
$n_{Bnp} * 1000$	213.05± 0.732	190.82± 0.643	150.13± 0.557	111.98± 0.487	80.67± 0.422
β_X	0.06± 0.045	0.15± 0.03	0.16± 0.031	0.21± 0.029	0.24± 0.03
β_ψ	0.36± 0.007	0.37± 0.005	0.4± 0.004	0.41± 0.004	0.45± 0.0
σ_{res}	0.02±0.0	0.02±0.0	0.02±0.0	0.02±0.0	0.02±0.0
σ_X	4.0±0.307	2.67±0.314	3.01±0.317	4.0±0.955	3.99±1.192
$\sigma_{\psi 1}$	2.52±0.049	4.26±0.215	4.49±0.208	2.36±0.079	2.48±0.043
$\sigma_{\psi 2}$	6.84±0.292	2.44±0.036	2.35±0.029	3.88±0.163	4.31±0.104
γ	0.7±0.302	0.3±0.007	0.3±0.005	0.39±0.057	0.5±0.0
Parameters	10-11	11-12	12-13	13-14	14-15
τ_ψ	1.48± 0.006	1.47± 0.007	1.49± 0.007	1.37± 0.007	1.43± 0.009
τ_1	0.33± 0.002	0.35± 0.002	0.31± 0.002	0.3± 0.003	0.27± 0.003
τ_2	1.53± 0.008	1.56± 0.009	1.5± 0.009	1.55± 0.01	1.42± 0.009
$n_X * 1000$	1.52± 0.152	1.22± 0.116	0.93± 0.146	0.65± 0.079	0.58± 0.069
$n_\psi * 1000$	21.86± 0.269	16.36± 0.181	13.48± 0.17	10.61± 0.179	8.05± 0.141
$n_{Bp} * 1000$	159.35± 0.504	104.81± 0.401	69.68± 0.351	47.48± 0.29	33.56± 0.25
$n_{Bnp} * 1000$	58.58± 0.362	41.64± 0.292	30.92± 0.261	22.6± 0.232	17.33± 0.207
β_X	0.27± 0.037	0.22± 0.038	0.31± 0.049	0.31± 0.055	0.3± 0.053
β_ψ	0.45± 0.0	0.48± 0.005	0.45± 0.0	0.51± 0.007	0.52± 0.008
σ_{res}	0.02±0.0	0.02±0.0	0.02±0.0	0.02±0.0	0.02±0.0
σ_X	4.0±1.195	4.0±0.297	3.99±0.974	4.0±1.084	4.0±0.16
$\sigma_{\psi 1}$	2.59±0.057	5.0±0.113	4.23±0.124	2.42±0.18	4.03±0.166
$\sigma_{\psi 2}$	4.14±0.121	2.8±0.053	2.4±0.055	4.05±0.28	2.41±0.092
γ	0.5±0.0	0.3±0.019	0.5±0.0	0.34±0.091	0.59±0.054

TABLE A.3: The parameters of the two-dimensional fit in m and t_z for different p_T bins in the rapidity bin $3.0 < y < 3.5$

Parameters	5-6	6-7	7-8	8-9	9-10
τ_ψ	1.44± 0.007	1.54± 0.007	1.52± 0.006	1.49± 0.006	1.46± 0.006
τ_1	0.44± 0.001	0.44± 0.001	0.42± 0.001	0.4± 0.001	0.38± 0.002
τ_2	1.64± 0.01	1.67± 0.009	1.64± 0.008	1.58± 0.008	1.59± 0.009
$n_X * 1000$	1.56± 0.408	2.55± 0.321	1.82± 0.411	2.19± 0.201	1.82± 0.159
$n_\psi * 1000$	19.27± 0.31	30.17± 0.372	32.05± 0.405	28.33± 0.254	23.81± 0.377
$n_{Bp} * 1000$	1283.92± 1.326	878.95± 1.098	549.54± 0.948	333.23± 0.685	204.09± 0.573
$n_{Bnp} * 1000$	214.75± 0.707	182.15± 0.609	134.23± 0.518	95.74± 0.433	66.8± 0.381
β_X	0.21± 0.066	0.07± 0.034	0.19± 0.056	0.19± 0.03	0.24± 0.033
β_ψ	0.45± 0.0	0.35± 0.004	0.38± 0.004	0.4± 0.004	0.42± 0.005
σ_{res}	0.02±0.0	0.02±0.0	0.02±0.0	0.02±0.0	0.02±0.0
σ_X	4.0±1.088	4.0±0.211	3.8±1.327	4.0±0.048	4.0±0.107
$\sigma_{\psi 1}$	3.66±0.149	2.67±0.045	2.78±0.046	2.8±0.03	2.86±0.098
$\sigma_{\psi 2}$	2.45±0.067	6.88±0.21	6.59±0.235	7.0±3.588	6.19±0.656
γ	0.5±0.0	0.69±0.018	0.7±0.017	0.7±0.01	0.69±0.056
Parameters	10-11	11-12	12-13	13-14	14-15
τ_ψ	1.47± 0.007	1.48± 0.008	1.47± 0.008	1.46± 0.01	1.38± 0.01
τ_1	0.36± 0.002	0.34± 0.002	0.34± 0.003	0.32± 0.003	0.31± 0.004
τ_2	1.53± 0.009	1.52± 0.009	1.53± 0.011	1.5± 0.011	1.51± 0.012
$n_X * 1000$	1.53± 0.147	0.84± 0.111	0.74± 0.092	0.68± 0.084	0.35± 0.065
$n_\psi * 1000$	17.75± 0.296	13.65± 0.191	10.92± 0.151	7.66± 0.121	5.89± 0.11
$n_{Bp} * 1000$	127.19± 0.461	80.9± 0.358	52.42± 0.29	35.11± 0.242	23.97± 0.204
$n_{Bnp} * 1000$	47.83± 0.323	34.07± 0.264	23.48± 0.221	17.07± 0.189	12.6± 0.164
β_X	0.19± 0.032	0.16± 0.049	0.22± 0.048	0.19± 0.044	0.17± 0.061
β_ψ	0.44± 0.005	0.45± 0.0	0.45± 0.0	0.49± 0.008	0.51± 0.009
σ_{res}	0.02±0.0	0.02±0.0	0.02±0.0	0.02±0.0	0.02±0.0
σ_X	4.0±1.19	3.99±1.076	4.0±1.471	4.0±1.386	2.97±0.558
$\sigma_{\psi 1}$	2.92±0.07	2.72±0.061	4.59±0.137	5.0±0.079	5.0±0.212
$\sigma_{\psi 2}$	5.28±0.571	4.89±0.145	2.5±0.059	3.02±0.17	3.21±0.179
γ	0.7±0.253	0.5±0.0	0.5±0.0	0.4±0.074	0.31±0.234

TABLE A.4: The parameters of the two-dimensional fit in m and t_z for different p_T bins in the rapidity bin $3.5 < y < 4.0$

Parameters	5-6	6-7	7-8	8-9	9-10
τ_ψ	1.61± 0.009	1.53± 0.009	1.49± 0.008	1.5± 0.008	1.56± 0.009
τ_1	0.5± 0.0	0.5± 0.001	0.49± 0.002	0.46± 0.002	0.45± 0.003
τ_2	1.6± 0.005	1.72± 0.014	1.71± 0.015	1.76± 0.014	1.66± 0.015
$n_X * 1000$	0.96± 3.109	1.59± 0.257	1.85± 0.204	1.45± 0.228	1.35± 0.13
$n_\psi * 1000$	15.05± 0.217	20.83± 0.347	20.33± 0.292	18.3± 0.376	13.99± 0.191
$n_{Bp} * 1000$	733.33± 2.726	519.59± 0.853	326.4± 0.676	199.84± 0.583	122.37± 0.418
$n_{Bnp} * 1000$	132.04± 0.407	110.94± 0.468	81.15± 0.391	57.76± 0.34	39.67± 0.27
β_X	0.18± 0.383	0.04± 0.044	0.11± 0.034	0.16± 0.039	0.16± 0.033
β_ψ	0.32± 0.006	0.33± 0.005	0.35± 0.005	0.37± 0.005	0.39± 0.006
σ_{res}	0.02±0.0	0.02±0.0	0.02±0.0	0.02±0.0	0.02±0.0
σ_X	3.51±0.918	4.0±1.029	4.0±0.255	4.0±1.49	4.0±0.94
$\sigma_{\psi 1}$	2.32±0.072	2.85±0.081	4.63±0.171	4.77±0.344	5.0±0.101
$\sigma_{\psi 2}$	4.55±0.096	6.83±0.221	2.43±0.06	2.46±0.062	3.36±0.068
γ	0.35±0.024	0.59±0.032	0.49±0.035	0.53±0.058	0.3±0.033
Parameters	10-11	11-12	12-13	13-14	14-15
τ_ψ	1.42± 0.008	1.44± 0.01	1.43± 0.011	1.39± 0.012	1.33± 0.014
τ_1	0.41± 0.003	0.39± 0.004	0.39± 0.005	0.39± 0.006	0.33± 0.006
τ_2	1.57± 0.014	1.61± 0.015	1.51± 0.016	1.46± 0.017	1.41± 0.018
$n_X * 1000$	0.96± 0.11	0.79± 0.079	0.41± 0.063	0.28± 0.052	0.27± 0.048
$n_\psi * 1000$	11.78± 0.203	8.6± 0.172	6.3± 0.127	4.4± 0.119	3.24± 0.084
$n_{Bp} * 1000$	74.17± 0.341	46.58± 0.272	29.89± 0.216	19.89± 0.179	13.15± 0.149
$n_{Bnp} * 1000$	27.14± 0.232	18.86± 0.194	13.12± 0.16	9.41± 0.137	6.64± 0.117
β_X	0.27± 0.042	0.21± 0.041	0.22± 0.058	0.15± 0.079	0.2± 0.066
β_ψ	0.41± 0.006	0.42± 0.007	0.44± 0.009	0.46± 0.01	0.47± 0.012
σ_{res}	0.02±0.0	0.02±0.0	0.02±0.0	0.02±0.0	0.02±0.0
σ_X	4.0±1.378	4.0±0.143	4.0±0.086	4.0±0.299	3.76±1.2
$\sigma_{\psi 1}$	2.6±0.119	3.11±0.102	4.8±0.188	3.33±0.098	3.37±0.103
$\sigma_{\psi 2}$	4.46±0.125	7.0±0.518	2.45±0.112	6.91±1.098	7.0±3.29
γ	0.3±0.058	0.67±0.039	0.62±0.045	0.7±0.4	0.7±0.085

TABLE A.5: The parameters of the two-dimensional fit in m and t_z for different p_T bins in the rapidity bin $4.0 < y < 4.5$

Parameters	5-6	6-7	7-8	8-9	9-10
τ_ψ	1.63± 0.023	1.46± 0.016	1.45± 0.015	1.34± 0.013	1.45± 0.017
τ_1	0.5± 0.0	0.5± 0.0	0.5± 0.001	0.03± 0.111	0.5± 0.002
τ_2	1.22± 0.011	1.36± 0.013	1.5± 0.016	1.0± 0.0	1.64± 0.023
$n_X * 1000$	0.4± 0.166	0.6± 0.132	0.61± 0.109	0.36± 0.082	0.29± 0.068
$n_\psi * 1000$	4.2± 0.163	6.41± 0.217	6.37± 0.194	4.86± 0.106	4.52± 0.135
$n_{Bp} * 1000$	207.58± 0.527	148.72± 0.458	96.17± 0.373	62.62± 0.285	37.06± 0.233
$n_{Bnp} * 1000$	35.49± 0.262	29.7± 0.236	21.95± 0.2	13.96± 0.154	10.74± 0.137
β_X	0.18± 0.113	0.04± 0.061	0.04± 0.057	0.01± 0.063	0.15± 0.082
β_ψ	0.27± 0.013	0.28± 0.01	0.29± 0.009	0.45± 0.0	0.32± 0.011
σ_{res}	0.02±0.0	0.02±0.0	0.02±0.0	0.02±0.0	0.02±0.0
σ_X	4.0±1.431	4.0±0.967	4.0±0.942	3.99±0.285	4.0±0.923
$\sigma_{\psi 1}$	3.08±0.384	2.75±0.172	3.19±0.164	5.0±0.054	3.21±0.19
$\sigma_{\psi 2}$	4.66±0.272	7.0±0.288	7.0±3.17	2.8±0.113	6.94±0.439
γ	0.3±0.033	0.43±0.045	0.54±0.056	0.5±0.0	0.49±0.057
Parameters	10-11	11-12	12-13	13-14	14-15
τ_ψ	1.43± 0.018	1.5± 0.022	1.47± 0.025	1.48± 0.029	1.35± 0.029
τ_1	0.5± 0.02	0.49± 0.011	0.43± 0.012	0.4± 0.014	0.35± 0.015
τ_2	1.51± 0.049	1.55± 0.041	1.42± 0.031	1.43± 0.034	1.23± 0.026
$n_X * 1000$	0.26± 0.054	0.24± 0.043	0.1± 0.027	0.04± 0.027	0.03± 0.02
$n_\psi * 1000$	3.34± 0.133	2.2± 0.078	1.69± 0.079	1.2± 0.056	0.82± 0.039
$n_{Bp} * 1000$	23.43± 0.198	14.66± 0.147	9.6± 0.122	6.07± 0.098	3.87± 0.078
$n_{Bnp} * 1000$	7.43± 0.127	5.04± 0.098	3.52± 0.084	2.39± 0.07	1.76± 0.058
β_X	0.21± 0.082	0.13± 0.071	0.2± 0.105	0.15± 0.315	0.03± 0.269
β_ψ	0.34± 0.012	0.37± 0.015	0.36± 0.017	0.38± 0.02	0.38± 0.023
σ_{res}	0.02±0.0	0.02±0.0	0.02±0.0	0.02±0.0	0.02±0.0
σ_X	4.0±0.223	4.0±0.316	2.5±1.328	4.0±1.048	4.0±0.923
$\sigma_{\psi 1}$	3.07±0.579	5.0±1.613	3.89±0.415	4.05±2.383	5.0±1.998
$\sigma_{\psi 2}$	5.92±1.044	4.5±0.212	7.0±1.122	6.19±4.192	4.76±0.837
γ	0.41±0.253	0.3±0.291	0.56±0.129	0.5±0.299	0.7±0.265

B References

[1] F. Englert and R. Brout, *Broken symmetry and the mass of gauge vector mesons*, Phys. Rev. Lett. **13** (1964) 321.

[2] P. W. Higgs, *Broken symmetries and the masses of gauge bosons*, Phys. Rev. Lett. **13** (1964) 508.

[3] Belle collaboration, S. K. Choi *et al.*, *Observation of a new narrow charmonium state in exclusive $B^+ \to K^+\pi^+\pi^- J/\psi$ decays*, Phys. Rev. Lett. **91** (2003) 262001, arXiv:hep-ex/0309032.

[4] R. F. Lebed, R. E. Mitchell, and E. S. Swanson, *Heavy-Quark QCD Exotica*, Prog. Part. Nucl. Phys. **93** (2017) 143, arXiv:1610.04528.

[5] LHCb collaboration, R. Aaij *et al.*, *Observation of $J/\psi\, p$ resonances consistent with pentaquark states in $\Lambda_b^0 \to J/\psi\, pK^-$ decays*, Phys. Rev. Lett. **115** (2015) 072001, arXiv:1507.03414.

[6] LHCb collaboration, R. Aaij *et al.*, *Observation of $X(3872)$ production in pp collisions at $\sqrt{s} = 7$ TeV*, Eur. Phys. J. **C72** (2012) 1972, arXiv:1112.5310.

[7] CMS collaboration, S. Chatrchyan *et al.*, *Measurement of the $X(3872)$ production cross section via decays to $J/\psi\,\pi^+\pi^-$ in pp collisions at $\sqrt{s} = 7$ TeV*, JHEP **04** (2013) 154, arXiv:1302.3968.

[8] ATLAS collaboration, M. Aaboud *et al.*, *Measurements of $\psi(2S)$ and $X(3872) \to J/\psi\,\pi^+\pi^-$ production in pp collisions at $\sqrt{s} = 8$ TeV with the ATLAS detector*, JHEP **01** (2017) 117, arXiv:1610.09303.

[9] A. Esposito *et al.*, *Observation of light nuclei at ALICE and the $X(3872)$ conundrum*, Phys. Rev. **D92** (2015), no. 3 034028, arXiv:1508.00295.

[10] W. Wang, *Comment on "Comment on 'Note on $X(3872)$ production at hadron colliders and its molecular structure' "*, arXiv:1709.10382; A. Esposito *et al.*, *Comment on 'Note on $X(3872)$ production at hadron colliders and its molecular structure'*, arXiv:1709.09631; M. Albaladejo *et al.*, *Note on $X(3872)$ production at hadron colliders and its molecular structure*, arXiv:1709.09101; C. Bignamini *et al.*, *Is the $X(3872)$ Production Cross Section at Tevatron Compatible with a Hadron Molecule Interpretation?*, Phys. Rev. Lett. **103** (2009) 162001, arXiv:0906.0882.

[11] Particle Data Group, C. Patrignani *et al.*, *Review of particle physics*, Chin. Phys. **C40** (2016) 100001, and 2017 update.

[12] LHCb collaboration, R. Aaij *et al.*, *Determination of the $X(3872)$ meson quantum numbers*, Phys. Rev. Lett. **110** (2013) 222001, arXiv:1302.6269; LHCb collaboration, R. Aaij *et al.*, *Quantum numbers of the $X(3872)$ state and orbital angular momentum in its $\rho^0 J/\psi$ decays*, Phys. Rev. **D92** (2015) 011102(R), arXiv:1504.06339.

[13] LHCb collaboration, R. Aaij *et al.*, *Measurement of B_c^+ production in proton-proton collisions at $\sqrt{s} = 8$ TeV*, Phys. Rev. Lett. **114** (2015) 132001, arXiv:1411.2943.

[14] C.-F. Qiao, P. Sun, D. Yang, and R.-L. Zhu, *B_c exclusive decays to charmonium and a light meson at next-to-leading order accuracy*, Phys. Rev. **D89** (2014) 034008, arXiv:1209.5859.

[15] LHCb collaboration, R. Aaij *et al.*, *Study of the kinematic dependences of Λ_b^0 production in pp collisions and a measurement of the $\Lambda_b^0 \to \Lambda_c^+ \pi^-$ branching fraction*, JHEP **08** (2014) 143, arXiv:1405.6842.

[16] LHCb collaboration, R. Aaij *et al.*, *Measurement of b hadron production fractions in 7 TeV pp collisions*, Phys. Rev. **D85** (2012) 032008, arXiv:1111.2357.

[17] LHCb collaboration, R. Aaij *et al.*, *Study of the productions of Λ_b^0 and $\overline{B}^0$ hadrons in pp collisions and first measurement of the $\Lambda_b^0 \to J/\psi\, pK^-$ branching fraction*, Chin. Phys. C **40** (2016) 011001, arXiv:1509.00292.

[18] LHCb collaboration, R. Aaij *et al.*, *Measurement of forward J/ψ production cross-sections in pp collisions at $\sqrt{s} = 13$ TeV*, JHEP **10** (2015) 172, Erratum ibid. **05** (2017) 063, arXiv:1509.00771.